

# Low Reynolds number gravitational settling of a sphere through a fluid-fluid interface: Modelling using a boundary integral method

Paul Jarvis<sup>\*1</sup>, Jon Blundy<sup>1</sup>, Katharine Cashman<sup>1</sup>, Herbert E Huppert<sup>1,2</sup>,  
and Heidy Mader<sup>1</sup>

<sup>1</sup>School of Earth Sciences, University of Bristol, Wills Memorial Building, Queens Road,  
Bristol, BS8 1RJ, UK

<sup>2</sup>Department of Applied Mathematics and Theoretical Physics, University of Cambridge,  
Wilberforce Road, Cambridge, CB3 0WA, UK

## Abstract

## 1 Introduction

## 2 Fundamentals of Stokes Flow

We present here a background to the fundamentals of Stokes flow, covering the equations of motion and non-dimensionalisation, different types of boundary condition, Greens functions and the integral representation of Stokes flow. Throughout this document we will

---

<sup>\*</sup>Corresponding author: paul.jarvis@bristol.co.uk

be making use of the Einstein summation convention and tensor notation (Riley et al., 2006).

## 2.1 Equations of Motion

The starting points for the majority of fluid dynamical problems are the continuity (equation 1) and Navier Stokes (equation 2) equations (Batchelor, 1967). Defining the fluid density  $\rho$ , the dynamic viscosity  $\eta$ , the fluid velocity field  $u_i$  and the pressure field  $P$  these are expressed as

$$\frac{\partial \rho(\mathbf{x}, t)}{\partial t} + \partial_i [\rho(\mathbf{x}, t) u_i(\mathbf{x}, t)] = 0, \quad (1)$$

and

$$\left( \frac{\partial [u_i(\mathbf{x}, t) \rho(\mathbf{x}, t)]}{\partial t} + [u_j(\mathbf{x}, t) \partial_j] [u_i(\mathbf{x}, t) \rho(\mathbf{x}, t)] \right) = -\partial_i P(\mathbf{x}, t) - \rho(\mathbf{x}, t) g + \eta \left( \partial_j \partial_j u_i(\mathbf{x}, t) + \frac{\partial_i (\partial_j u_j(\mathbf{x}, t))}{3} \right). \quad (2)$$

Forming a coupled set of non-linear, partial differential equations for the velocity and pressure fields as functions of space  $\mathbf{x}$  and time  $t$ , these represent mass and momentum conservation respectively, and must be satisfied by all Newtonian fluid phases within the system. For most practical applications, the fluids are assumed to be incompressible (have constant density) and so the continuity equation reduces to the incompressibility relation;

$$\partial_i u_i(\mathbf{x}, t) = 0. \quad (3)$$

This can be combined with equation 2 to give the incompressible Navier Stokes equation;

$$\rho \left( \frac{\partial u_i(\mathbf{x}, t)}{\partial t} + [u_j(\mathbf{x}, t) \partial_j] u_i(\mathbf{x}, t) \right) = -\partial_i P(\mathbf{x}, t) - \rho g + \eta \partial_j \partial_j u_i(\mathbf{x}, t). \quad (4)$$

The equations of motion can be expressed in an alternative form by defining the stress tensor  $T_{ij}(\mathbf{x}, t)$  (Batchelor, 1967; Manga, 1994) and dynamic pressure  $P_d(\mathbf{x}, t)$ :

$$T_{ij}(\mathbf{x}, t) = -P_d(\mathbf{x}, t)\delta_{ij} + \eta[\partial_i u_j(\mathbf{x}, t) + \partial_j u_i(\mathbf{x}, t)], \quad (5)$$

$$P_d(\mathbf{x}, t) = P(\mathbf{x}, t) - \rho g_i x_i, \quad (6)$$

where  $\delta_{ij}$  are the components of the Kronecker delta tensor. This definition of the stress tensor removes the gravitational body force from the equations of motion, meaning that it only appears in the boundary conditions. The Navier Stokes equation then becomes

$$\rho \left( \frac{\partial u_i(\mathbf{x}, t)}{\partial t} + [u_j(\mathbf{x}, t)\partial_j]u_i(\mathbf{x}, t) \right) = \partial_j T_{ij}(\mathbf{x}, t). \quad (7)$$

When working in fluid dynamics, it is usual to non-dimensionalise the equations of motion and boundary conditions (White, 1999). This can be achieved by scaling the quantities involved by parameters specific to the problem. For example, consider a problem with typical scales of length  $L_c$  and velocity  $U_c$ . This allows us to define dimensionless variables (denoted by a ')

$$x_i = L_c x'_i, \quad (8)$$

$$u_i(\mathbf{x}, t) = U_c u'_i(\mathbf{x}', t'), \quad (9)$$

and

$$t = \frac{L_c t'}{U_c}. \quad (10)$$

In the case of highly viscous flows the relevant scaling for the dynamic pressure uses a characteristic viscosity  $\eta_c$  and is given by (Lee and Leal, 1982)

$$P_d(\mathbf{x}, t) = \frac{\eta_c U_c P'_d(\mathbf{x}', t')}{L_c}. \quad (11)$$

This choice of pressure scaling means that upon substitution of equations 8 to 11 into equation 5, the stress tensor can also be non-dimensionalised,

$$T_{ij}(\mathbf{x}, t) = \frac{\eta_c U_c T'_{ij}(\mathbf{x}', t')}{L_c}, \quad \text{where} \quad T'_{ij}(\mathbf{x}', t') = P'_d(\mathbf{x}', t')\delta_{ij} + \Lambda[\partial'_i u'_j(\mathbf{x}', t') + \partial'_j u'_i(\mathbf{x}', t')], \quad (12)$$

where  $\Lambda = \eta/\eta_c$ . Hence, the dimensionless continuity and Navier Stokes equations are

$$\partial'_i u'_i(\mathbf{x}', t') = 0, \quad (13)$$

and

$$Re \left( \frac{\partial u'_i(\mathbf{x}', t')}{\partial t'} + (u'_j(\mathbf{x}', t')\partial'_j)u'_i(\mathbf{x}', t') \right) = \partial'_j T'_{ij}(\mathbf{x}', t'), \quad (14)$$

where the Reynolds number  $Re$  is defined as

$$Re = \frac{\rho L_c U_c}{\eta_c} \quad (15)$$

As we are considering the case of low Reynolds number ( $Re \ll 1$ ), we can neglect the inertial terms on the right hand side, and the equation reduces to the Stokes equation (Batchelor, 1967; Kim and Karrila, 2005)

$$\partial'_i T'_{ij}(\mathbf{x}') = 0. \quad (16)$$

Note that the explicit time dependence has now vanished from the Stokes equations. However, it is still valid to use the equations for time dependent flows where the boundary conditions change with time, if the quasi-static assumption is satisfied;

$$\frac{L_c^2 \rho}{\eta_c} \ll \tau \quad (17)$$

where  $\tau$  is a typical timescale for a change in flow geometry. Physically, this means that the velocity and stress fields of the fluid instantaneously respond to changes in the boundary conditions (Manga, 1994).

## 2.2 Boundary Conditions

In order to complete the formulation of any fluid dynamics problem, it is necessary to state the boundary conditions alongside the equations of motion (Riley et al., 2006). For fluids of infinite (or semi-infinite) extent in some dimension, these include the flow velocity at infinity. For bounded flows, the conditions are imposed at the boundaries of the fluid domain, and their exact nature depends on the phase of the material bounding it. At a boundary, two types of boundary condition can exist: a kinematic boundary condition on the velocity field and a dynamic boundary condition on the stress field (derivative of the velocity field). Kinematic boundary conditions are an expression of mass conservation and dynamic boundary conditions are a balance of forces, an expression of Newton's third law. Geometric symmetries can be exploited to identify further boundary conditions and reduce the complexity of problems. In unsteady flows, initial conditions are also important, but since we are considering quasi-static flows, we will not discuss these here.

### 2.2.1 Fluid-Solid Boundary

At low Reynolds number, for a fluid-solid boundary defined the surface  $\mathcal{S}$  (see figure 1), the kinematic boundary condition usually employed is one of no-slip; the fluid velocity at the boundary is the same as that of the solid  $U'_{s,i}$ . This is easily expressed in dimensionless

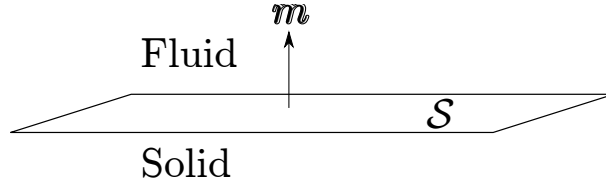


Figure 1: Fluid-solid boundary  $\mathcal{S}$  with normal vector  $\mathbf{m}$  directed into the fluid phase.

form as

$$u'_i(\mathbf{x}') = U'_{s,i}, \quad \text{when } \mathbf{x} \in \mathcal{S}. \quad (18)$$

This is valid for situations when the fluid domain is much larger than the mean free path of molecules within the fluid. When this isn't true, a slip condition can be employed at the boundary (Dussan, 1976). There also needs to be a dynamic boundary condition applied at the interface. If the solid exerts a force  $F_i$  onto the fluid, then the condition states

$$\int_{\mathcal{S}} m_i(\mathbf{x}) T_{ij}(\mathbf{x}) d\mathcal{S} = F_j, \quad (19)$$

where  $m_i(\mathbf{x})$  is the normal vector to  $\mathcal{S}$  directed into the fluid. Using the non-dimensionalisation scheme presented above this becomes

$$\eta_c U_c L_c \int_{\mathcal{S}} f_i(\mathbf{x}') d\mathcal{S}' = F_i, \quad (20)$$

where  $f_i(\mathbf{x}') = m_i(\mathbf{x}') T'_{ij}(\mathbf{x}')$  is defined as the dimensionless traction vector on the surface  $\mathcal{S}$ .

### 2.2.2 Fluid-Fluid Boundary

For a boundary  $\mathcal{I}$  between two fluids labelled 1 and 2 (figure 2), the usual kinematic boundary condition states that the velocity of the two fluids must be continuous across

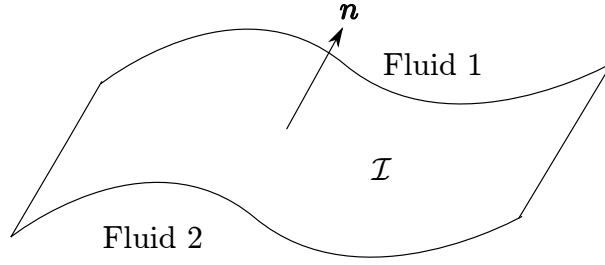


Figure 2: Fluid-fluid boundary  $\mathcal{I}$  with normal vector  $\mathbf{n}$ .

the interface (Kim and Karrila, 2005). Defining the velocity of fluid  $l$  as  $u_l$  this can be expressed in dimensionless form as

$$u'_{1,i}(\mathbf{x}') = u'_{2,i}(\mathbf{x}'), \quad \text{for } \mathbf{x}' \in \mathcal{I}. \quad (21)$$

Again, when fluid domains are small compared to the mean free path of molecules a slip condition can be employed (Maxwell, 1879). The dynamic boundary condition is an expression of the balance between the stress discontinuity across the interface and the interfacial tension (IFT)  $\sigma$  (Batchelor, 1967). With our definition of the stress tensor this is given as (Manga, 1994)

$$\begin{aligned} n_i(\mathbf{x})[T_{1,ij}(\mathbf{x}) - \rho_1 g_k x_k \delta_{ij}] - n_i(\mathbf{x})[T_{2,ij}(\mathbf{x}) - \rho_2 g_k x_k \delta_{ij}] = \\ \sigma(\mathbf{x})n_j(\mathbf{x})[\partial_{s,i}n_i(\mathbf{x})] - \partial_{s,j}\sigma(\mathbf{x}), \quad \text{for } \mathbf{x} \in \mathcal{I}, \end{aligned} \quad (22)$$

where  $n_i$  is the normal vector to the surface  $\mathcal{I}$  directed into fluid 1. The operator  $\partial_{s,i}$  is defined as the tangential gradient operator within the surface  $\mathcal{I}$ :

$$\partial_{s,i} = (\delta_{ij} - \partial_i \partial_j) \partial_j. \quad (23)$$

When this takes the normal vector as its argument it can be shown that (Brackbill et al.,

1992)

$$\partial_{s,i} n_i = \partial_i n_i. \quad (24)$$

The presence of spatial gradients in the interfacial tension can lead to so-called Marangoni effects (Thomson, 1855; Gibbs, 1878). However, for our purposes we will assume that the interfacial tension is uniform across the interface  $\mathcal{I}$ , and so the last term on the right hand side vanishes;

$$\begin{aligned} n_i(\mathbf{x})[T_{1,ij}(\mathbf{x}) - \rho_1 g_k x_k \delta_{ij}] - n_i[T_{2,ij}(\mathbf{x}) - \rho_2 g_k x_k \delta_{ij}] = \\ \sigma(\mathbf{x}) n_i(\mathbf{x}) \partial_i n_j(\mathbf{x}), \quad \text{for } \mathbf{x} \in \mathcal{I}. \end{aligned} \quad (25)$$

Like the equations of motion, this can be non-dimensionalised using equations 8 to 12

$$n_i(\mathbf{x}') [T'_{1,ij}(\mathbf{x}') - T'_{2,ij}(\mathbf{x}')] Ca + Bo(\hat{z}_i x'_i) n_j(\mathbf{x}') = n_j(\mathbf{x}') \partial'_i n_i(\mathbf{x}') \quad \text{for } \mathbf{x}' \in \mathcal{I}. \quad (26)$$

The capillary number  $Ca$  and Bond number  $Bo$  are dimensionless numbers defined as:

$$Ca = \frac{\eta_c U_c}{\sigma}, \quad (27)$$

and

$$Bo = \frac{(\rho_2 - \rho_1) g L_c^2}{\sigma}. \quad (28)$$

## 2.3 Greens functions

In order to derive the integral representation of the Stokes equations, it is necessary to make use of the Greens functions (Riley et al., 2006) for Stokes flow,  $\hat{u}_i(\mathbf{x}' - \mathbf{y}')$  and



$\hat{T}_{ij}(\mathbf{x}' - \mathbf{y}')$ , defined such that (Kim and Karrila, 2005)

$$\partial'_i \hat{u}_i(\mathbf{x}' - \mathbf{y}') = 0, \quad (29)$$

and

$$\partial'_i \hat{T}_{ij}(\mathbf{x}' - \mathbf{y}') + \mathcal{F}_j \delta(\mathbf{x}' - \mathbf{y}') = 0, \quad (30)$$

where  $\mathcal{F}_i$  is a arbitrary constant vector,  $\delta(\mathbf{x}' - \mathbf{y}')$  is the Dirac delta-function (appendix A) and both  $\hat{u}_i(\mathbf{x}')$  and  $\hat{T}_{ij}(\mathbf{x}') \rightarrow 0$  as  $|\mathbf{x}'| \rightarrow \infty$ . Equations 29 and 30 can be solved following Ladyzhenskaya (1963) to show that (see appendix B) (Kim and Karrila, 2005)

$$\hat{u}_j(\boldsymbol{\xi}) = \frac{\mathcal{F}_i J_{ij}(\boldsymbol{\xi})}{\Lambda}, \quad (31)$$

and

$$\hat{T}_{ij}(\boldsymbol{\xi}) = K_{ijk}(\boldsymbol{\xi}) \mathcal{F}_k, \quad (32)$$

where  $\boldsymbol{\xi} = \mathbf{x}' - \mathbf{y}'$ ,

$$J_{ij}(\boldsymbol{\xi}) = \frac{1}{8\pi\xi} \left( \delta_{ij} + \frac{\xi_i \xi_j}{\xi^2} \right), \quad (33)$$

and

$$K_{ijk}(\boldsymbol{\xi}) = \frac{-3\xi_i \xi_j \xi_k}{4\pi\xi^5}. \quad (34)$$

We have defined  $\xi = \xi_i \xi_i$ .

## 2.4 Integral Representation of Stokes Equations

We now substitute the Greens functions and unknown velocity and stress field solutions into the Lorentz Reciprocal Theorem (equation 125 in appendix C) and simplify using equations 16 and 30 to find

$$\oint_{\mathcal{V}} u'_k(\mathbf{x}') \delta(\boldsymbol{\xi}) d\mathbf{x}'^3 = \frac{1}{\Lambda} \oint_{\mathcal{S}} J_{ik}(\boldsymbol{\xi}) T'_{ij}(\mathbf{x}') n_j(\mathbf{x}') d\mathbf{x}'^2 - \oint_{\mathcal{S}} u'_i(\mathbf{x}') K_{ijk}(\boldsymbol{\xi}) n_j(\mathbf{x}') d\mathbf{x}'^2. \quad (35)$$

Here the integrals are defined in the sense of the Cauchy Principle Value (CPV) to account for the possibility that the kernels  $J_{ij}$  and  $K_{ijk}$  have singular points in the range of integration. Finally make the transformation  $\mathbf{x}' \leftrightarrow \mathbf{y}'$  and use the symmetry properties of the kernels (equations 111 and 112 in appendix B) and the delta function (equation 88 in appendix A) to obtain the general form of the integral representation of the Stokes equations;

$$\oint_{\mathcal{V}} u'_k(\mathbf{y}') \delta(\boldsymbol{\xi}) d\mathbf{y}'^3 = \frac{1}{\Lambda} \oint_{\mathcal{S}} J_{ik}(\boldsymbol{\xi}) T'_{ij}(\mathbf{y}') n_j(\mathbf{y}') d\mathbf{y}'^2 + \oint_{\mathcal{S}} u'_i(\mathbf{y}') K_{ijk}(\boldsymbol{\xi}) n_j(\mathbf{y}') d\mathbf{y}'^2. \quad (36)$$

Using the definition of the delta function (equation 86 in appendix A) this means

$$\frac{1}{\Lambda} \oint_{\mathcal{S}} J_{ik}(\boldsymbol{\xi}) T'_{ij}(\mathbf{y}') n_j(\mathbf{y}') d\mathbf{y}'^2 + \oint_{\mathcal{S}} u'_i(\mathbf{y}') K_{ijk}(\boldsymbol{\xi}) n_j(\mathbf{y}') d\mathbf{y}'^2 = \begin{cases} u'_k(\mathbf{x}') & \mathbf{x}' \in \mathcal{V} \\ \frac{u'_k(\mathbf{x}')}{2} & \mathbf{x}' \in \mathcal{S} \\ 0 & \text{otherwise} \end{cases}. \quad (37)$$

### 3 Theoretical Development

#### 3.1 Problem Statement

We are interested in the low Reynolds number, on-axis gravitational settling of a spheroid towards a fluid-fluid interface (figure 3). We denote the upper(lower) phase as fluid 1(2). The physical parameters motivate the choice of scaling variables. The characteristic lengthscale is chosen to be the horizontal minor axis  $a$ , characteristic viscosity that of the upper fluid  $\eta_1$ , and characteristic velocity to be the terminal velocity of a sphere of radius  $a$  in the upper fluid(Reynolds, 1886)

$$U_c = \frac{2(\rho_s - \rho_1)ga^2}{9\eta_1}, \quad (38)$$

where  $\rho_1$  is the density of fluid 1,  $\rho_s$  the spheroid density, and  $g = 9.81 \text{ m s}^{-2}$  the acceleration due to gravity. Defining  $\rho_2$  as the density of fluid 2 and  $\sigma$  as the IFT, this means the capillary and Bond numbers can be expressed as

$$Ca = \frac{(\rho_s - \rho_1)ga^2}{\sigma}, \quad (39)$$

and

$$Bo = \frac{(\rho_2 - \rho_1)ga^2}{\sigma}. \quad (40)$$

The dimensionless stress tensor for each fluid can be written as

$$T'_{\alpha,ij}(\mathbf{x}') = -P'_{d,l}(\mathbf{x}')\delta_{ij} + \Lambda_l[\partial'_i u'_{l,j}(\mathbf{x}') - \partial'_j u'_{l,i}(\mathbf{x}')], \quad (41)$$

where  $P'_{d,l}$  and  $u'_{l,i}$  are the dimensionless dynamic pressure and velocity fields in fluid  $l$  respectively. We use  $l$  to denote the fluid and  $i, j$  to denote tensoral components. The

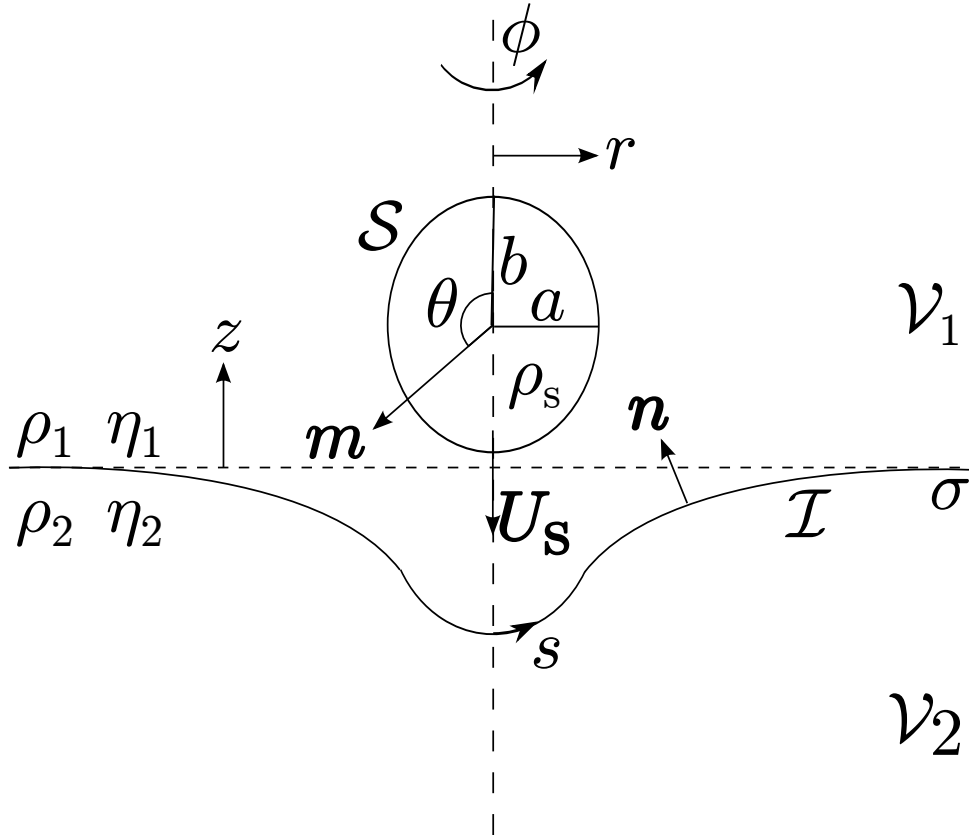


Figure 3: Diagrammatic representation of the system. A spheroid falls on-axis under gravity, at low Reynolds number, towards an initially horizontal interface between two density stratified, immiscible, semi-infinite fluids.

parameter  $\Lambda_l$  is defined as

$$\Lambda_l = \frac{\eta_l}{\eta_1} = \begin{cases} 1, & l = 1 \\ \frac{\eta_2}{\eta_1} = \lambda, & l = 2 \end{cases}. \quad (42)$$

where  $\eta_2$  is the dynamic viscosity of the lower phase. Note  $\lambda$  is the viscosity ratio of the two fluids. Additionally  $\mathcal{V}_{1(2)}$  denotes the volume of fluid 1(2),  $\mathcal{I}$  the interface and  $\mathcal{S}$  the spheroid surface.  $\mathbf{m}$  and  $\mathbf{n}$  are the normal vectors to the spheroid surface and interface respectively and both are directed into fluid 1. We use cylindrical polar coordinates to describe the system with  $r$  the radial coordinate with respect to the symmetry axis,  $\phi$  the azimuthal coordinate, and  $z$  the vertical coordinate with respect to the plane of the initial, undeformed interface. Additionally we make use of the polar angle  $\theta$  defined with respect to the centre of the spheroid, and the arc-length  $s$  defined as the distance along the interface from the symmetry axis in any azimuthal plane.

It is straightforward to apply the general equations of motion and boundary conditions to the problem. The equations of motion, which must be satisfied in both fluid domains, appear as

$$\partial'_1 u'_{l,i}(\mathbf{x}') = 0, \quad (43)$$

and

$$\partial'_1 T'_{l,ij}(\mathbf{x}') = 0. \quad (44)$$

The first boundary condition that we impose is that the undisturbed fluid is quiescent, so the velocity field is constrained to decay away from the sphere;

$$u'_{l,i}(\mathbf{x}') \rightarrow 0 \text{ as } |\mathbf{x}'| \rightarrow \infty. \quad (45)$$

The kinematic boundary condition on the fluid interface (equation 21) can be expressed as

$$u'_{1,i}(\mathbf{x}') = u'_{2,i}(\mathbf{x}'), \quad \mathbf{x}' \in \mathcal{I}. \quad (46)$$

The dynamic boundary condition is also imposed at the interface;

$$n_i(\mathbf{x}') [T'_{1,ij}(\mathbf{x}') - T'_{2,ij}(\mathbf{x}')] Ca + \hat{z}_i x'_i n_j(\mathbf{x}') Bo = n_j(\mathbf{x}') \partial'_i n_i(\mathbf{x}'), \quad \text{for } \mathbf{x}' \in \mathcal{I}. \quad (47)$$

However we can define the modified density ratio (MDR)  $D$  as

$$D = \frac{Ca}{Bo} = \frac{\rho_s - \rho_1}{\rho_2 - \rho_1}. \quad (48)$$

This means equation 47 can be re-expressed as

$$n_i(\mathbf{x}') [T'_{1,ij}(\mathbf{x}') - T'_{2,ij}(\mathbf{x}')] D Bo = n_j(\mathbf{x}') [\partial'_i n_i(\mathbf{x}') - \hat{z}_i x'_i Bo], \quad \text{for } \mathbf{x}' \in \mathcal{I}. \quad (49)$$

The kinematic boundary condition on the spheroid surface is

$$u'_{1,i}(\mathbf{x}') = U'_{s,i}, \quad \mathbf{x}' \in \mathcal{S}. \quad (50)$$

where  $U_{s,i}$  is the velocity of the spheroid. The final boundary condition is the dynamic boundary condition on the spheroid. The force on the fluid due to the spheroid originates from the balance between gravity and buoyancy;

$$F_i = -\frac{4\pi a^2 b (\rho_s - \rho_1) g \hat{z}_i}{3}, \quad (51)$$

where  $b$  is the vertical minor axis. Substituting this into equation 20 and using equation 38 we obtain

$$\int_{\mathcal{S}} f_i(\mathbf{x}') d\mathcal{S}' = -6\pi \hat{z}_i. \quad (52)$$

Defining the aspect ratio of the spheroid  $R = b/a$ , the dimensionless numbers that describe the system are the set  $\{\lambda, D, Bo, R\}$ .

### 3.2 Integral Representation

To recast the problem in an integral representation, we need to apply equation 37 to each fluid separately. The domain of fluid 1 is bound by the spheroid surface and interface, and extends to infinity as  $r, z \rightarrow \infty$ . The boundary condition at infinity (equation 45) ensures that the far-field contribution to the surface integrals in equation 37 vanishes, meaning that just the spheroid surface and interface contribute. Additionally the no-slip boundary condition on the spheroid surface (equation 50), the divergence theorem (appendix E) and the definition of the Greens function for pressure (equation 30) can be used to show that the integral of  $u'_{1,i}(\mathbf{y}') K_{ijk}(\boldsymbol{\xi}) m_j(\mathbf{y}')$  over the spheroid surface vanishes. Hence the boundary integral equation for fluid 1 can be written as

$$\begin{aligned} & \oint_{\mathcal{S}} J_{ik}(\boldsymbol{\xi}) T'_{1,ij}(\mathbf{y}') m_j(\mathbf{y}') d^2 \mathbf{y}' + \oint_{\mathcal{I}} J_{ik}(\boldsymbol{\xi}) T'_{1,ij}(\mathbf{y}') n_j(\mathbf{y}') d^2 \mathbf{y}' + \\ & \oint_{\mathcal{I}} u'_{1,i}(\mathbf{y}') K_{ijk}(\boldsymbol{\xi}) n_j(\mathbf{y}') d^2 \mathbf{y}' = \begin{cases} \frac{u'_{1,k}(\mathbf{x}')}{2} & \mathbf{x}' \in \mathcal{I} \\ u'_{s,k} & \mathbf{x}' \in \mathcal{S} \end{cases}. \end{aligned} \quad (53)$$

For fluid 2, the contribution to the surface integrals at infinity again vanishes leaving just a contribution from the interface. Using the kinematic boundary condition at the interface

(equation 46) the boundary integral equation for fluid 2 can be written as

$$-\oint_{\mathcal{I}} J_{ik}(\boldsymbol{\xi}) T'_{1,ij}(\mathbf{y}') n_j(\mathbf{y}') d^2 \mathbf{y}' - \lambda \oint_{\mathcal{I}} u'_{1,i}(\mathbf{y}') K_{ijk}(\boldsymbol{\xi}) n_j(\mathbf{y}') d^2 \mathbf{y}' = \frac{\lambda u'_{1,k}(\mathbf{x}')}{2} \quad \mathbf{x}' \in \mathcal{I}, \quad (54)$$

where the minus sign occurs since the normal vector is directed out of fluid 2. Equations 53 and 54 can be added together and combined with equation 49 to obtain

$$\begin{aligned} & \oint_{\mathcal{S}} J_{ik}(\boldsymbol{\xi}) f_{s,i}(\mathbf{y}') d^2 \mathbf{y}' + \frac{9}{2DBo} \oint_{\mathcal{I}} J_{ik}(\boldsymbol{\xi}) n_i(\mathbf{y}') [\partial'_j n_j(\mathbf{y}') - \hat{z}_j y'_j Bo] d^2 \mathbf{y}' + \\ & (1 - \lambda) \oint_{\mathcal{I}} u'_{1,i}(\mathbf{y}') K_{ijk}(\boldsymbol{\xi}) n_j(\mathbf{y}') d^2 \mathbf{y}' = \begin{cases} \frac{(1+\lambda)u'_{1,k}(\mathbf{x}')}{2} & \mathbf{x}' \in \mathcal{I} \\ u'_{s,k} & \mathbf{x}' \in \mathcal{S} \end{cases}. \end{aligned} \quad (55)$$

This together with equation 52 completely describes the system in an integral representation.

### 3.3 Axisymmetric Simplification

We can exploit the axial symmetry of the system to chose the point  $\mathbf{x}'$  such that it lies in the plane defined by  $\phi = 0$ . Hence in Cartesian coordinates  $\mathbf{x}' = (x_r, 0, x_z)$ . This also means we can write  $\mathbf{y}' = (y_r \cos \phi, y_r \sin \phi, y_z)$ . On the surface of the spheroid  $y_r = y_r(\theta)$  and  $y_z = y_z(\theta)$ , and on the interface  $y_r = y_r(s)$  and  $y_z = y_z(s)$ . Additionally  $\mathbf{f} = [f_r(\theta) \cos \phi, f_r(\theta) \sin \phi, f_z(\theta)]$  and  $\mathbf{n} = [n_r(s) \cos \phi, n_r(s) \sin \phi, n_z(s)]$ . Since the system is axisymmetric, it is useful to extract the azimuthal integration from the surface integrals in equations 52 and 55. To achieve this, the Cartesian components of each equation are considered separately. For equation 55, it can be shown that both the left and right hand sides of the 2-component equation are identically zero. For equation 52 this is true for the 1- and 2-components. To show this,  $J_{ij}$  and  $K_{ijk}$  are first expanded in terms of in terms of the components of  $\mathbf{x}'$  and  $\mathbf{y}'$  before the integration over  $\phi$  is carried out. This leaves three integral equations which can be expressed as



$$\begin{aligned}
R \int_{\theta=0}^{\pi} B_{\alpha\beta}(\mathbf{x}', \theta) \Phi_{\beta}(\theta) d\theta + \int_{s=0}^{\infty} \left( A_{\alpha\beta}(\mathbf{x}', s) y_r(s) - \frac{(1+\lambda)\delta_{\alpha\beta}\delta(s-s_0)}{2} \right) \Psi_{\beta}(s) ds \\
= - \int_{s=0}^{\infty} C_{\alpha}(\mathbf{x}', s) y_r(s) ds, \quad \text{for } \mathbf{x}' \in \mathcal{I}, \quad (56)
\end{aligned}$$

$$R \int_{\theta=0}^{\pi} B_{\alpha\beta}(\mathbf{x}', \theta) \Phi_{\beta}(\theta) d\theta + \int_{s=0}^{\infty} A_{\alpha\beta}(\mathbf{x}', s) \Psi_{\beta}(s) y_r(s) ds - \Theta_{\alpha} = \int_{s=0}^{\infty} C_{\alpha}(\mathbf{x}', s) y_r(s) ds, \quad \text{for } \mathbf{x}' \in \mathcal{S}, \quad (57)$$

and

$$\int_{\theta=0}^{\pi} \Phi_2(\theta) d\theta = -3, \quad (58)$$

where the quantities  $\mathbf{A}$ ,  $\mathbf{B}$ ,  $\mathbf{C}$ ,  $\Psi$ ,  $\Phi$  and  $\Theta$  are defined as:

$$\mathbf{A} = (1-\lambda) \int_{\phi=0}^{2\pi} \begin{pmatrix} n_r(K_{111} \cos^2 \phi + K_{221} \sin^2 \phi + 2K_{121} \sin \phi \cos \phi) & n_r(K_{131} \cos \phi + K_{231} \sin \phi) \\ + n_z(K_{131} \cos \phi + K_{231} \sin \phi) & + n_z K_{331} \\ n_r(K_{113} \cos^2 \phi + K_{223} \sin^2 \phi + 2K_{123} \sin \phi \cos \phi) & n_r(K_{133} \cos \phi + K_{233} \sin \phi) \\ + n_z(K_{133} \cos \phi + K_{233} \sin \phi) & + n_z K_{333} \end{pmatrix} d\phi, \quad (59)$$

$$\mathbf{B} = \int_{\phi=0}^{2\pi} \begin{pmatrix} J_{11} \cos \phi + J_{21} \sin \phi & J_{31} \\ J_{13} \cos \phi + J_{23} \sin \phi & J_{33} \end{pmatrix} d\phi, \quad (60)$$

$$\mathbf{C} = \frac{9(\partial'_j n_j - \text{Bo} y_z)}{2D\text{Bo}} \int_{\phi=0}^{2\pi} \begin{pmatrix} n_r(J_{11} \cos \phi + J_{21} \sin \phi) + n_z J_{31} \\ n_r(J_{13} \cos \phi + J_{23} \sin \phi) + n_z J_{23} \end{pmatrix} d\phi, \quad (61)$$

$$\Psi = \begin{pmatrix} u'_{1,r}(s) \\ u'_{1,z}(s) \end{pmatrix}, \quad (62)$$

$$\Phi = \begin{pmatrix} f_{s,r}(\theta) \\ f_{s,z}(\theta) \end{pmatrix} \sin^2 \theta \left( 1 + \frac{\cot^2 \theta}{R^2} \right)^{1/2}, \quad (63)$$

and

$$\Theta = \begin{pmatrix} 0 \\ u'_s \end{pmatrix} \quad (64)$$

For brevity, the function arguments have been dropped from the kernels and the normal vectors but  $n_i = n_i[\mathbf{y}'(s, \phi)]$  and in equation 59,  $K_{ijk} = K_{ijk}[\mathbf{x}' - \mathbf{y}'(s, \phi)]$ , in equation 60,  $J_{ij} = J_{ij}[\mathbf{x}' - \mathbf{y}'(\theta, \phi)]$  and in equation 61,  $J_{ij} = J_{ij}[\mathbf{x}' - \mathbf{y}'(s, \phi)]$ .

The azimuthal integrals inside the definitions of  $\mathbf{A}$ ,  $\mathbf{B}$  and  $\mathbf{C}$  can be expressed as sums of complete elliptic integrals of the first and second kind (Lee and Leal, 1982; Geller et al., 1985; Graziani, 1989; Pozrikids, 1992; Manga, 1994; Roumeliotis, 2000) which can then be evaluated using polynomial expansions (Abramowitz and Stegun, 1972). Details of this are given in appendices F and G.

## 4 Numerical Method

Equations 56 to 58 are a coupled set of integral equations for the unknowns  $\Psi(s)$ ,  $\Phi(\theta)$  and  $\Theta$ . These solutions can be found numerically by discretising the system, allowing the integral equations to be expressed as a linear system of algebraic equations which are then solved using LU decomposition and Gaussian elimination (Riley et al., 2006; Press et al., 2007). Once the interfacial and sphere velocities are solved for, the system is iterated forward in time, and the process is repeated.

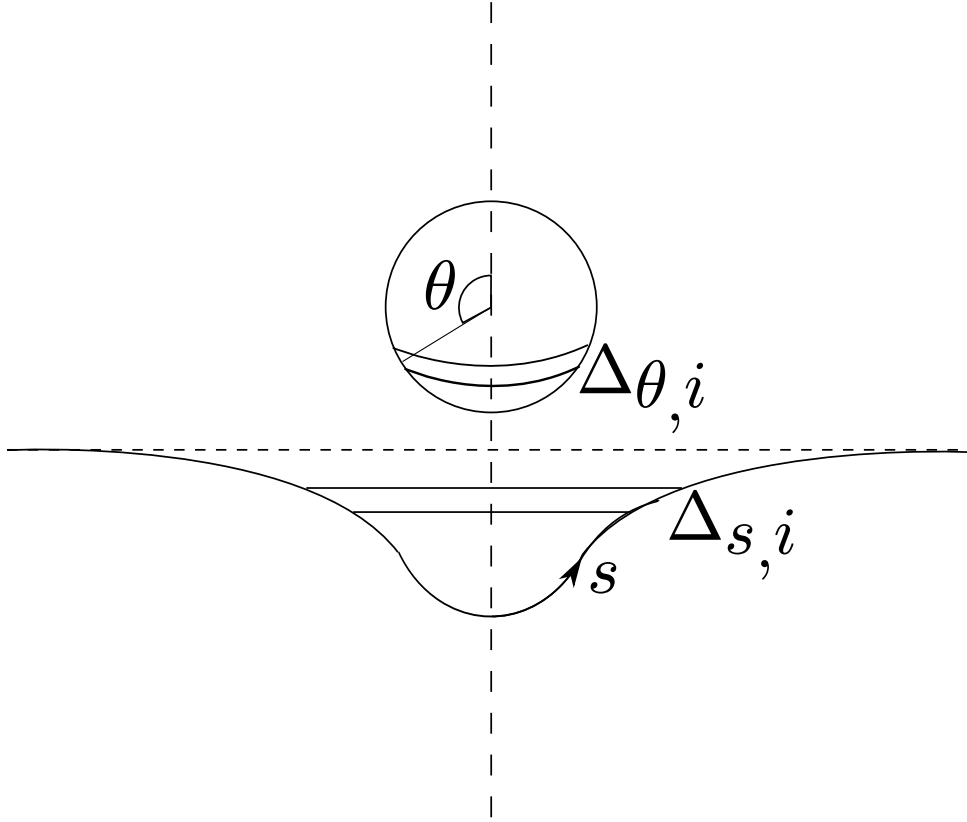


Figure 4: Diagrammatic representation of the discretisation of the system. Both interface and spheroid surface are divided into axisymmetric rings centred on the symmetry axis.

#### 4.1 Discretisation and Linear System

To discretise the set of equations, the interface and sphere surface are divided into intervals. The interface is divided into  $N$  axisymmetric rings, where the  $i^{\text{th}}$  ring is centred at arc-length  $s_i$  and is of thickness  $\Delta_{s,i}$ . The interface is truncated at the arc-length  $s_N$ . The sphere surface is discretised in  $M$  axisymmetric rings, where the  $i^{\text{th}}$  ring is centred at polar coordinate  $\theta_i$  and has a thickness  $\Delta_{\theta,i}$ . A schematic of the discretisation scheme is depicted in figure 4.

We now choose  $\mathbf{x}' = \mathbf{x}_i$  where  $\mathbf{x}_i = \mathbf{x}_i(\theta_i)$  on  $\mathcal{S}$  and  $\mathbf{x}_i = \mathbf{x}_i(s_i)$  on  $\mathcal{I}$ . That is, the point  $\mathbf{x}'$  is chosen to be the midpoint of one of the intervals. Then, we can express the integrals as discrete sums over each element. We then make the approximation that the unknowns  $\Psi(s)$  and  $\Phi(\theta)$  are constant over the width of an interval and for interval  $i$ ,  $\Psi(s) = \Psi(s_i)$

and  $\Phi(\theta) = \Phi(\theta_i)$ . This allows us to obtain the discrete form of the integral equations:

$$\begin{aligned} R \sum_{i=1}^M \Phi_\beta(\theta_i) \int_{\Delta_{\theta,i}} B_{\alpha\beta}(s_j, \theta) d\theta + \sum_{i=1}^N \Psi_\beta(s_i) \int_{\Delta_{s,i}} \left( A_{\alpha\beta}(s_j, s) y_r(s) - \frac{(1+\lambda)\delta_{\alpha\beta}\delta(s-s_j)}{2} \right) ds \\ = - \sum_{i=1}^N \int_{\Delta_{s,i}} C_\alpha(s_j, s) y_r(s) ds, \end{aligned} \quad (65)$$

$$R \sum_{i=1}^M \Phi_\beta(\theta_i) \int_{\Delta_{\theta,i}} B_{\alpha\beta}(\theta_j, \theta) d\theta + \sum_{i=1}^N \Psi_\beta(s_i) \int_{\Delta_{s,i}} A_{\alpha\beta}(\theta_j, s) y_r(s) ds - \Theta_\alpha = - \sum_{i=1}^N \int_{\Delta_{s,i}} C_\alpha(\theta_j, s) y_r(s) ds, \quad (66)$$

and

$$\sum_{i=1}^M \Phi_2(\theta_i) \int_{\Delta_{\theta,i}} d\theta = -3. \quad (67)$$

This is seemingly a set of  $2(N+M)+1$  linear equations for  $2(N+M)+1$  unknowns;  $\Phi_\alpha(\theta_i)$ ,  $\Psi_\alpha(s_j)$  and  $\Theta_1$  (recall that  $\Theta_2 = 0$ ) where  $\alpha = 1, 2$ ,  $i = 1, 2, \dots, M$  and  $j = 1, 2, \dots, N$ . However we can use physical arguments to simplify the system further. First by symmetry, the radial interfacial velocity must vanish on the symmetry axis i.e.  $\Psi_1(s_1) = 0$ . Additionally, the on-axis radial tractions on the sphere must also vanish meaning  $\Phi_1(\theta_1) = \Phi_1(\theta_M) = 0$ . Indeed, it can be shown that the coefficients of these terms vanish by using the expressions for  $A_{\alpha\beta}$ ,  $B_{\alpha\beta}$  and  $C_\alpha$ , given in appendix G.1. Hence the equations where these terms appear are redundant and can be removed from the linear system. This leaves us with a system of  $2(N+M-1)$  linear equations for  $2(N+M-1)$  unknowns.

## 4.2 Evaluation of the coefficients

These equations can be recast as a matrix equation  $L_{\mu\nu} X_\mu = Y_\nu$  where the unknown quantities are the elements  $X_\mu$ . The elements  $L_{\mu\nu}$  and  $Y_\nu$  are the coefficients of the

Table 1: The order of the singularity of the components of  $\mathbf{A}$ ,  $\mathbf{B}$  and  $\mathbf{C}$ .

$A_{11}$	$1/\epsilon$	$B_{11}$	$\ln  \epsilon $	$C_1$	$\ln  \epsilon $
$A_{12}$	0	$B_{12}$	0	$C_2$	$\ln  \epsilon $
$A_{21}$	0	$B_{21}$	0		
$A_{22}$	0	$B_{22}$	$\ln  \epsilon $		

system and contain integrals that need to be evaluated numerically. If  $\mathbf{x}'_j$  is not within the range of integration, then this is done using 4-point Gaussian-Legendre quadrature (Riley et al., 2006). However if  $\mathbf{x}'_j$  is in the integration range, then the integrand is singular at the point  $\mathbf{y}' = \mathbf{x}'_j$  and care needs to be taken when evaluating the integral. First, the order of the singularity needs to be determined. To do this, write  $\mathbf{y}' = \mathbf{x}'_j + \epsilon \mathbf{t}$ , where  $\epsilon = \theta - \theta_j$  on the sphere, and  $\epsilon = s - s_j$  on the interface, and  $\mathbf{t}$  is the tangent to the curve. The integrands are then expanded in terms of  $\epsilon$ . The order of the singularity is the order of the first order singular term in  $\epsilon$ . Table 1 shows the order of the singularity of each component of  $\mathbf{A}$ ,  $\mathbf{B}$  and  $\mathbf{C}$ .

We then re-write the integrand as the sum of a regular and singular part. Denoting the integrand by  $I(\zeta, \zeta_i)$  (where  $\zeta$  represents  $\theta$  or  $s$  depending on whether the integration is over the sphere or the interface) this can be written as  $I(\zeta, \zeta_i) = I_r(\zeta, \zeta_i) + I_s(\zeta, \zeta_i)$  where  $I_r$  is the regular part and  $I_s$  is the singular part. The singular part can then be written as

$$I(\zeta, \zeta_i)_s = [I_s(\zeta, \zeta_i) - L(\zeta, \zeta_i)] + L(\zeta, \zeta_i), \quad (68)$$

where  $L$  is the leading order contribution to  $I_s$ . The terms in square parentheses now form a regular function which can be integrated numerically. For the case that the integral is  $1/\epsilon$  singular, the final term can be expressed as

$$L(\zeta, \zeta_i) = \frac{g(\zeta, \zeta_i)}{\epsilon} = \frac{g(\zeta, \zeta_i) - g(\zeta_i, \zeta_i)}{\epsilon} + \frac{g(\zeta_i, \zeta_i)}{\epsilon}. \quad (69)$$

Similarly, if the integral is singular

$$L(\zeta, \zeta_i) = g(\zeta, \zeta_i) \ln |\epsilon| = [g(\zeta, \zeta_i) - g(\zeta_i, \zeta_i)] \ln |\epsilon| + g(\zeta_i, \zeta_i) \ln |\epsilon| \quad (70)$$

In both these cases, the first term on the right hand side is regular and the last term is singular but can be integrated analytically. This means that the irregular integrand can be expressed as the sum of a regular function, that can be integrated numerically, and an irregular function, that can be integrated analytically.

To calculate integrals over the interface, it is necessary to evaluate the components of the normal vector and its divergence at discrete points along the interface. To do this, cubic splines are fitted to the collocation points describing the interface (WAITING FOR DE BOER BOOK TO REF THIS) using routines given in Press et al. (2007) so that the interface is described parametrically with  $r = r(s)$  and  $z = z(s)$ . Remembering that for a surface  $H(r, z) = z - f(r)$ , the components of the normal vector are given by  $n_i = \partial_i H / (\partial_j H \partial_j H)$  (Riley et al., 2006), the following expressions can be obtained

$$n_r(s) = \frac{-\dot{z}}{(\dot{r} + \dot{z})^{1/2}}, \quad (71)$$

$$n_z(s) = \frac{\dot{r}}{(\dot{r} + \dot{z})^{1/2}}, \quad (72)$$

and

$$\partial'_i n_i = \frac{\dot{z}}{r(\dot{r} + \dot{z})^{1/2}} + \frac{\dot{r}\ddot{z} - \ddot{r}\dot{z}}{(\dot{r} + \dot{z})^{3/2}}. \quad (73)$$

These expressions are given in given in (Manga, 1994) except for a minus sign error in the components of the normal. The derivatives of the splines are calculated numerically using routines modified from Press et al. (2007). Once all of the elements  $L_{\mu\nu}$  and  $Y_\nu$  have been calculated the system of equations is solved by Lower-Upper (LU) decomposition

and Gaussian elimination (Riley et al., 2006; Press et al., 2007) using routines from the GNU Scientific Library (GSL) (Galassi et al., 2009).

### 4.3 Temporal Iteration

The system is iterated forward in time using an explicit first order Euler method (Manga, 1994) with timestep  $\Delta t$ . This means the position of the sphere  $z_s$  at time  $t + \Delta t$  is found using

$$z_s(t' + \Delta t') = U'_s(t)\Delta t', \quad (74)$$

and the position of the collocation points on the interface moves according to

$$x_r(s_i, t' + \Delta t') = u_r(s_i, t')\Delta t', \quad (75)$$

and

$$x_z(s_i, t' + \Delta t') = u_z(s_i, t')\Delta t'. \quad (76)$$

There are both numerical and physical constraints on the value of the timestep. Numerically, it is limited by the Courant-Friedrich-Lewy (CFL) criterion Courant28. Physically, it is necessary to ensure that it is smaller than the timescale over which different processes can occur. Owing to the multi-component nature of this problem, there are four timescales intrinsic to the problem: the Stokes timescale in the upper fluid  $\tau_{s,1} = 9\eta_1/[2(\rho_s - \rho_1)ga]$ , the Stokes timescale in the lower fluid  $\tau_{s,2} = 9\eta_2/[2(\rho_s - \rho_2)ga]$ , the capillary time for the upper fluid  $\tau_{c,1} = \eta_1 a/\sigma$  and the capillary time for the lower fluid  $\tau_{c,2} = \eta_2 a/\sigma$ . It is required that the timestep is smaller than all of these so that the physics occurring on each timescale can be resolved. Non-dimensionalising each of these timescales we find that in dimensionless form they exist as  $\tau'_{s,1} = 1$ ,  $\tau'_{s,2} = \lambda D/(D - 1)$ ,  $\tau'_{c,1} = 2DBo/9$ ,

$\tau'_{c,2} = 2DBo\lambda/9$ . Hence, for each simulation, the shortest physical timescale is identified and the timestep is constrained to be smaller than this throughout the simulation. The timestep is allowed to change during the simulation such that it is as large as can be allowed by both the CFL and numerical criteria.

Due to gradients in the velocity tangential to the fluid interface, the distribution of collocation points is altered during this time stepping process, so the collocation points are redistributed between each time step. Following the redistribution, the linear system is reconstructed for the new geometry and solved using the same procedure. The process continues in this fashion until the separation between the sphere and the interface, or two different parts of the interface equals the local separation between collocation points, as the discretisation no longer provides an accurate approximation to the continuous system

## 5 Model Testing

### 5.1 Uniform and Infinite Fluid

To test the model, we can remove the interface and fluid 2, leaving us with the problem of the steady gravitational settling of a spheroid through fluid 1, which is uniform and infinite in extent. The terminal velocity of a spheroid settling on axis can be solved for analytically (Happel and Brenner, 1973) and in our dimensionless scheme is given by

$$U'_t = \frac{1}{K}, \tag{77}$$

where

$$K = \begin{cases} \frac{4}{3(\mu^2+1)^{1/2}[\mu-(\mu^2-1)\cot^{-1}\mu]} & \text{for } R < 1 \\ \frac{4}{3(\mu^2-1)^{1/2}[(\mu^2+1)\coth^{-1}\mu-\mu]} & \text{for } R > 1 \\ 1 & \text{for } R = 1, \end{cases} \tag{78}$$



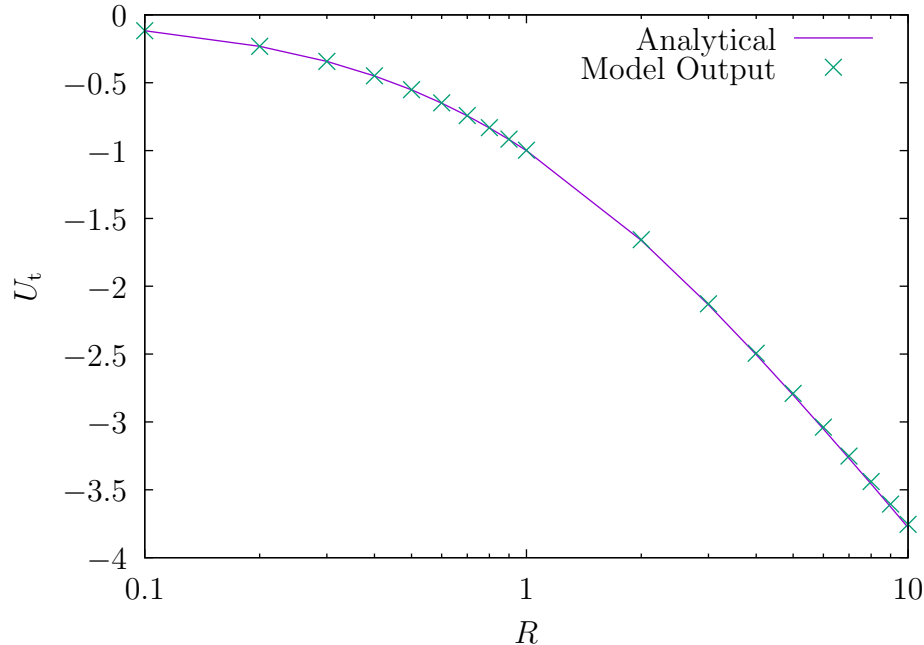


Figure 5: Curve shows analytical solution for dimensionless terminal velocity vs. aspect ratio (equation 78). Points show calculated values from model. There is excellent agreement for oblate spheroids but the error increases with aspect ratio.

and

$$\mu = \frac{R}{|R^2 - 1|^{1/2}}. \quad (79)$$

For the case that  $\lambda = 1$ , and a flat interface, the integrals over the interface in equations 65 to 67 vanish and the system reduces to that of the case of a spheroid settling in an infinite and uniform fluid. Figure 5 shows the analytical result for the terminal velocity from Happel and Brenner (1973) compared with that calculated by our model. It can be seen that agreement is excellent for aspect ratios in the range 0.1-10.

We tested the sensitivity of the results to the number of intervals on the sphere. Figure 6 shows the fractional error on the calculated terminal velocity as a function of the number of intervals used to discretise the sphere  $M$ , for both a prolate and oblate spheroid, and a sphere. For  $M \geq 100$ , the fractional error is less than 0.003. It is also clear here that the error increases with  $R$ .

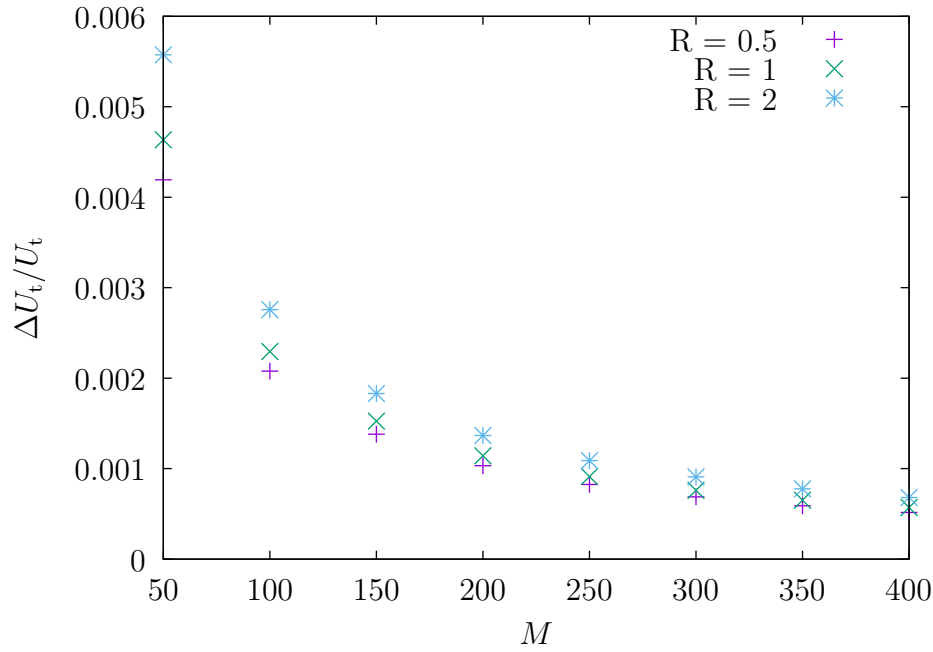


Figure 6: Plot showing the fractional error on the calculated terminal velocity of a spheroid in an infinite and uniform fluid as a function of the number of intervals used to discretise the particle surface. Results are shown for  $R = 0.5, 1$  and  $2$ . When 100 intervals are used, the fractional error is less than 0.003 and this decreases as the number of intervals increases. It can also be seen that as  $R$  increases so does the error.

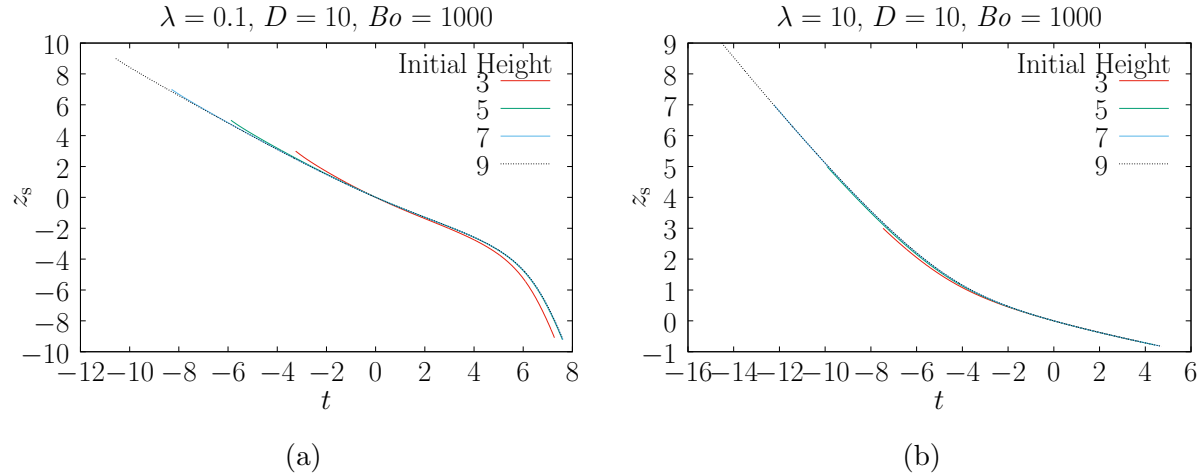


Figure 7: Plot of the vertical position of a sphere versus time for different initial sphere positions for  $D = 10$  and  $Bo = 1000$ . a)  $\lambda = 0.1$  - For initial positions greater or equal than 5 radii above the interface, the position curves quickly converge. b)  $\lambda = 10$  - For initial positions greater or equal than 5 radii above the interface, the position curves are indistinguishable. For an initial position of 3, the curve quickly converges to the others.

## 5.2 Initial Height of Sphere

The interface will deform as the particle approaches and so we require the initial position of the particle to be far enough above the interface that the results are insensitive to the initial position. We tested the model for parameter values  $R = 1$ ,  $D = 10$ ,  $Bo = 1000$  and both  $\lambda = 0.1$  and  $\lambda = 10$ . Figure 7 shows the position of the sphere against time for the different viscosity ratios. The time  $t = 0$  is defined as the moment when  $z_s = 0$ . It is seen that the position curves converge for an initial position greater than or equal to 5 sphere radii above the interface. Figure 8 shows that the same is true when considering the volume of upper phase fluid entrained below the plane  $z = 0$ .

## 5.3 Truncation Length

The model is also tested for its sensitivity with respect to the radial coordinate  $r = r_N$  at which the interface is truncated. Figure 9 shows the position of the sphere as a function

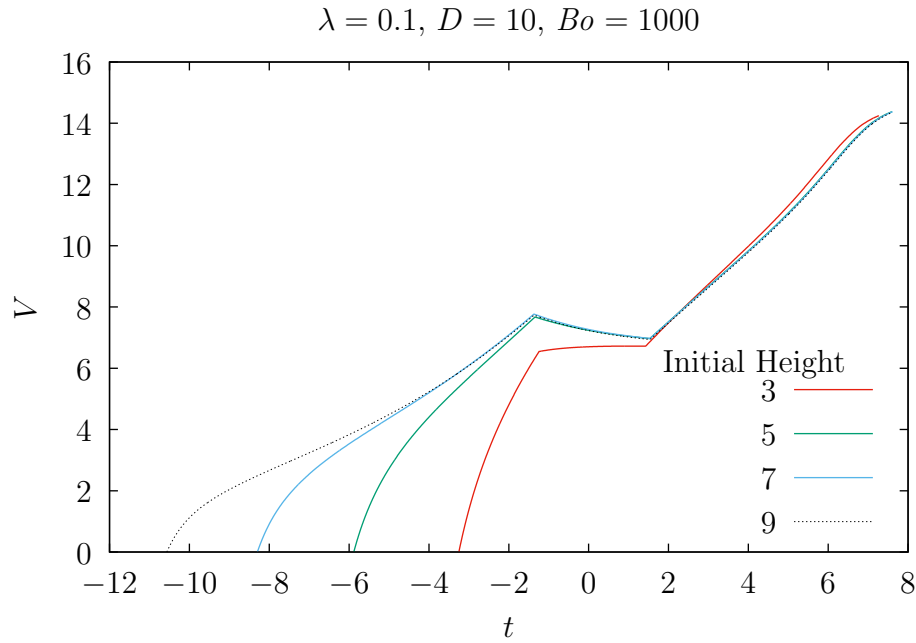


Figure 8: Curves showing the volume of upper phase fluid entrained below the plane  $z = 0$  as a function of time, for different initial sphere positions and  $D = 10$ ,  $Bo = 1000$  and  $\lambda = 0.1$ . It is seen that the curves converge for an initial position greater than or equal to 5 sphere radii above the interface.

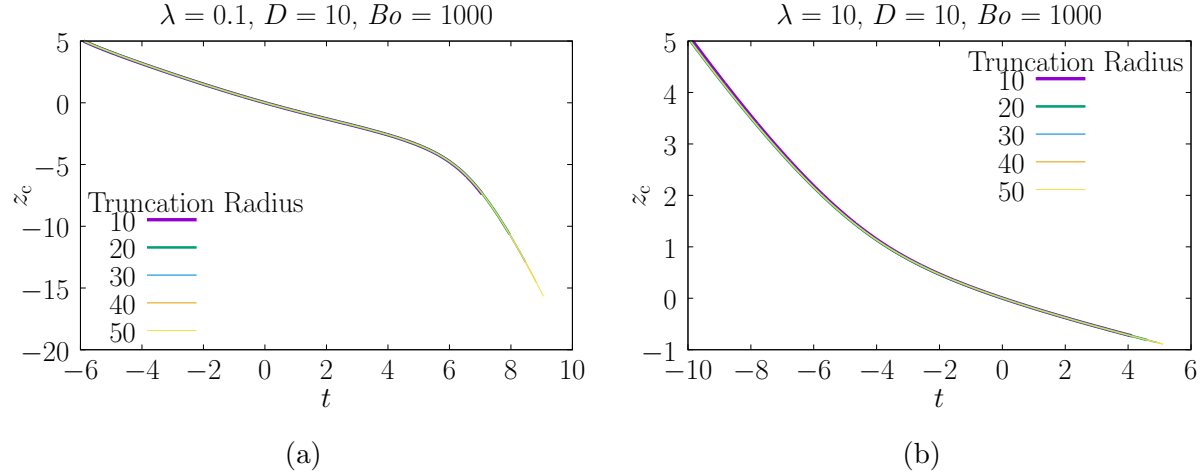


Figure 9: Plot of the vertical position of a sphere versus time for different truncation radii for  $D = 10$ ,  $Bo = 1000$  and both  $\lambda = 0.1$  (a) and  $\lambda = 10$  (b). The curves are identical for all truncation radii greater than or equal to 10.

of time for different  $r_N$ . It is seen that for  $r_N \geq 10$  there is no change to the results. Figure 10 shows the dependence of the entrained volume as a function of time on the truncation radius. For  $r_N \geq 20$  the curves are identical from the start of the simulation, and for  $r_N = 10$  the curve converges to the others during the run.

## 5.4 Discretisation of Interface

The number of elements used to discretise the fluid interface  $N$  needs to be large enough that the model output is independent of  $N$ . Figure 11 shows the vertical position of the sphere as a function of time for different  $N$ . It can be seen that for  $N \geq 50$  the curves are independent of  $N$ . However, the larger the value of  $N$  the longer the duration of the simulation. This is because larger values of  $N$  allow smaller separations between surfaces to be tolerated.

Figure 12 shows the effect of  $N$  on the time dependence of the volume of upper phase fluid entrained beneath the plane  $z = 0$ . As with the position curves, these are seen to be independent of  $N$  for  $N \geq 50$ .

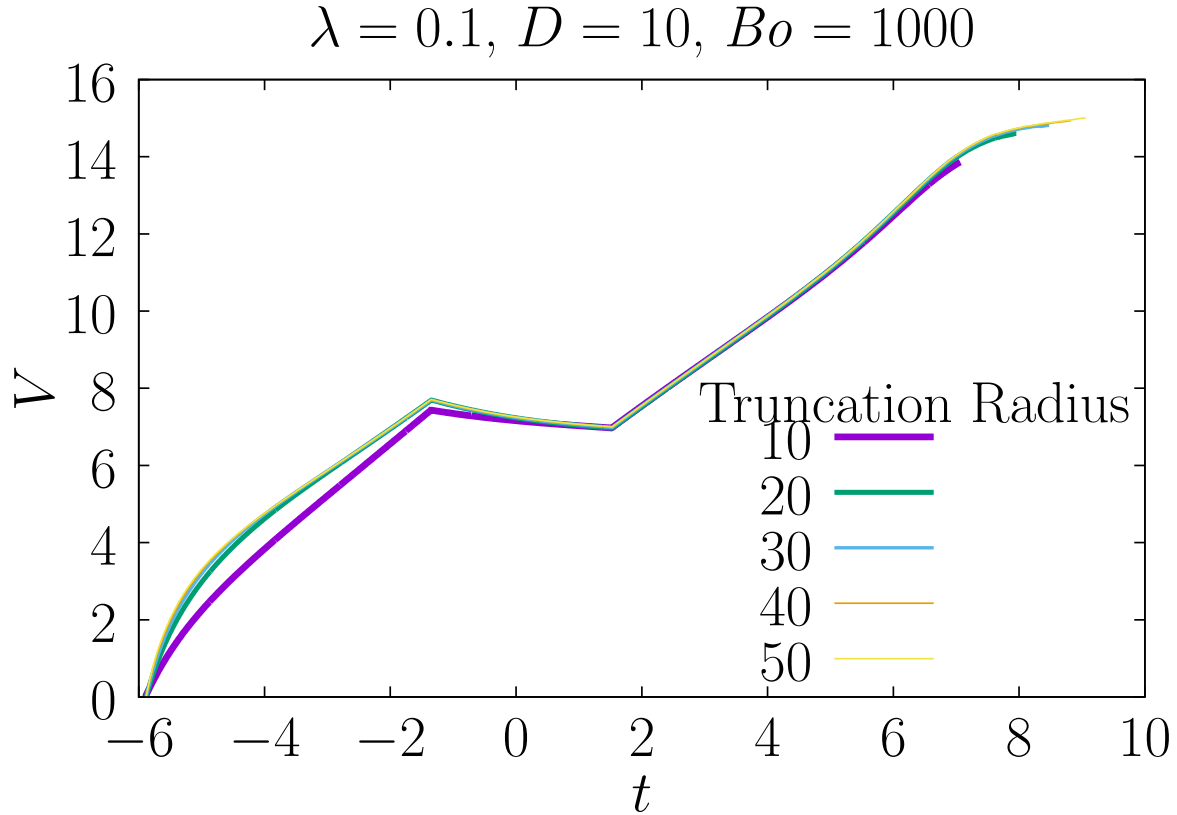


Figure 10: Curves showing the volume of upper phase fluid entrained below the plane  $z = 0$  as a function of time, for different truncation radii and  $D = 10$ ,  $Bo = 1000$  and  $\lambda = 0.1$ . It is seen that the curves for  $r_N \geq 20$  are identical from the start of the simulation, although the curve for  $r_N = 10$  converges to the other curves during the run.

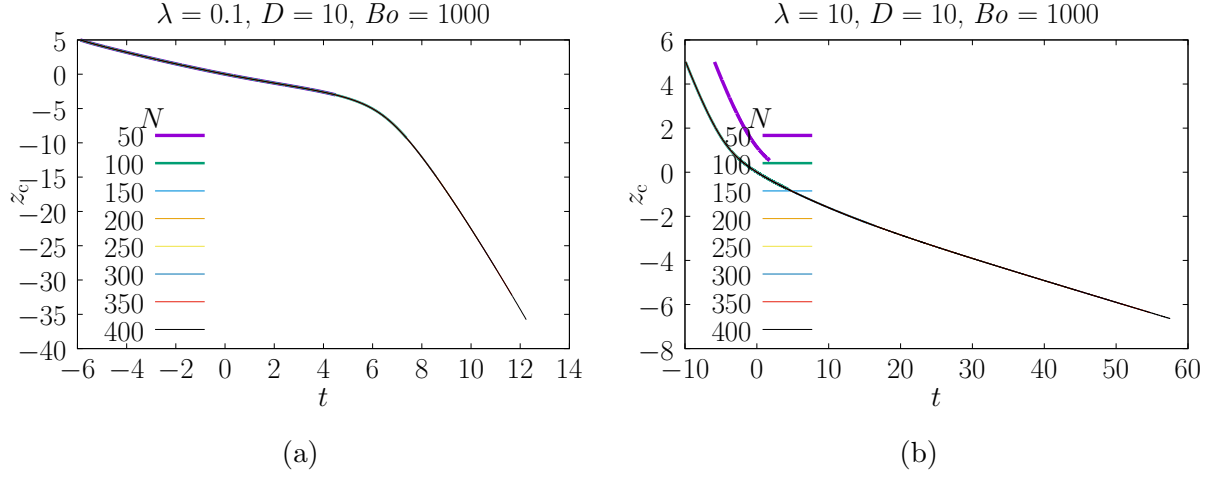


Figure 11: Vertical position of the sphere versus time for different numbers of elements used to discretise the interface  $N$  for  $D = 10$ ,  $Bo = 1000$  and both (a)  $\lambda = 0.1$  and (b)  $\lambda = 10$ . The curves are identical for all choices of  $N \geq 50$ . However, the larger the value of  $N$  the longer the duration of the simulation.

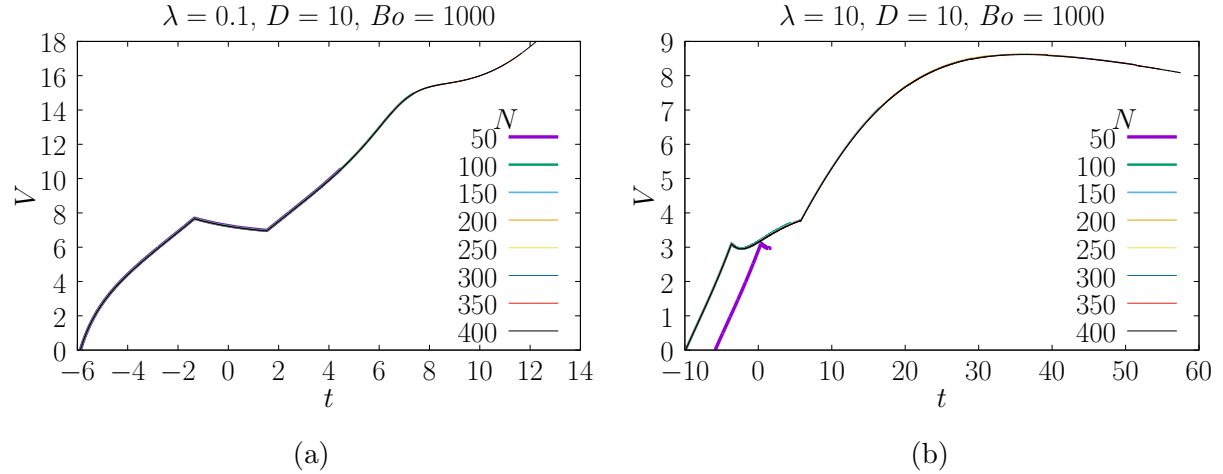


Figure 12: Volume of upper phase fluid entrained below the plane  $z = 0$  as a function of time for different numbers of elements used to discretise the interface  $N$  for  $D = 10$ ,  $Bo = 1000$  and both (a)  $\lambda = 0.1$  and (b)  $\lambda = 10$ . The curves are identical for all choices of  $N \geq 50$ .

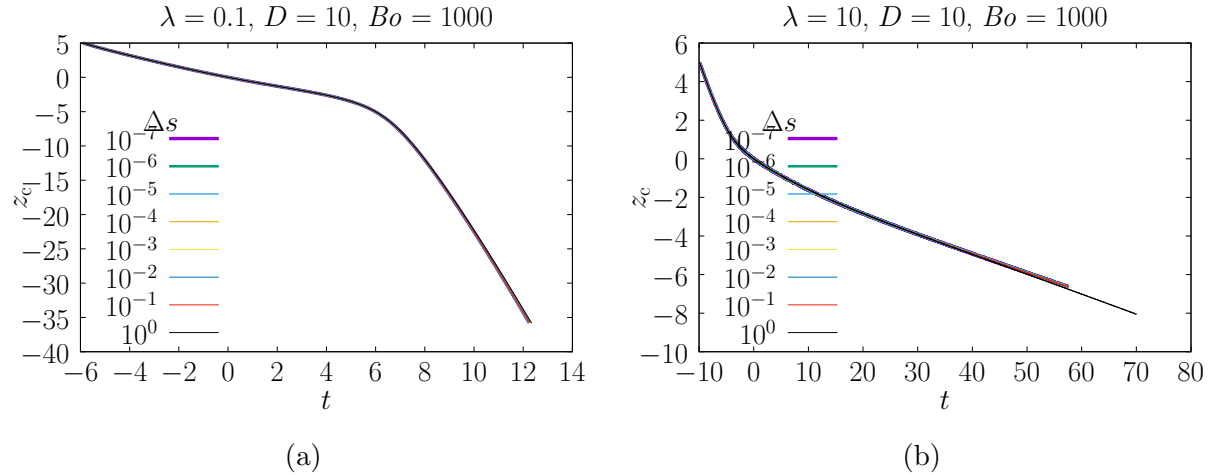


Figure 13: Vertical position of the sphere versus time for different values of the initial step size for numerical differentiation for  $D = 10$ ,  $Bo = 1000$  and both (a)  $\lambda = 0.1$  and (b)  $\lambda = 10$ . The curves are identical for all choices of  $\Delta s \leq 0.1$ .

## 5.5 Numerical Differentiation of Interface

At each timestep it is necessary to differentiate the functions  $r(s)$  and  $z(s)$  that describe the interface as a function of arc-length (subsection 4.2). The numerical differentiation routines used require the choice of an initial step-size  $\Delta s$  (Press et al., 2007). The sensitivity of the model to this choice has been investigated and it is shown that results are independent of  $\Delta s$  for  $\Delta s \leq 0.1$  (figures 13 and 14).



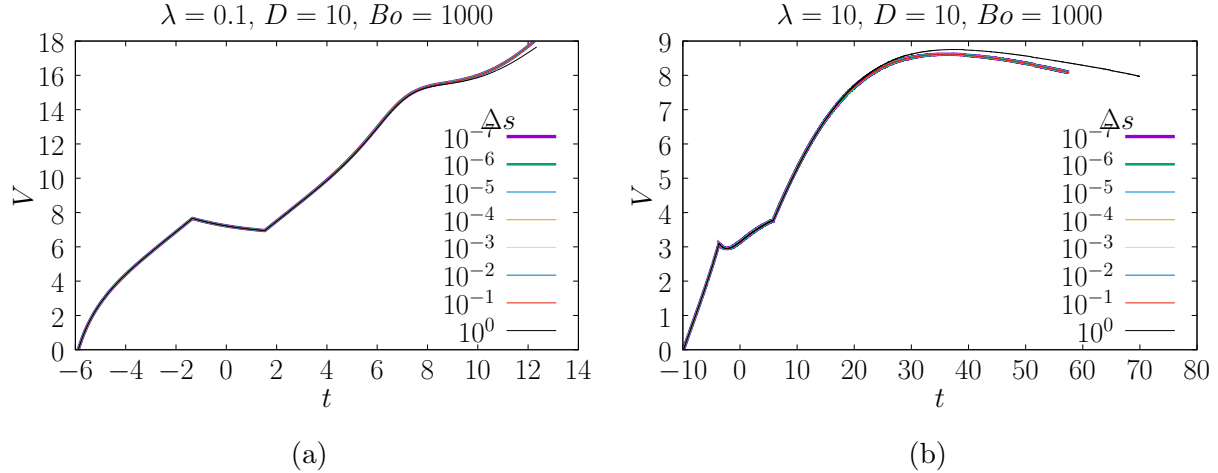


Figure 14: Time dependence of volume of upper phase fluid entrained below the plane  $z = 0$  for different values of the initial step size for numerical differentiation for  $D = 10$ ,  $Bo = 1000$  and both (a)  $\lambda = 0.1$  and (b)  $\lambda = 10$ . The curves are identical for all choices of  $\Delta s \leq 0.1$ .

## 5.6 Experimental Verification

# 6 Results

## 6.1 Settling Spheres

### 6.1.1 Floating versus Sinking

There are two possible situations for each simulation: floating or sinking. For simulations where floating is observed, the sphere velocity becomes negligibly small as the sphere-interface separation decreases, and never increases. This leads to the sphere attaining an equilibrium position at the interface (figures 15 and 16). Alternatively, the sphere velocity can remain significant at all times, and the interface deforms around the sphere as it sinks through the interface (figures 17 and 18).

A regime diagram has been constructed for the floating-sinking transition. It has been found that for  $\lambda \leq 10$  the location of the transition in the parameter space defined by  $D$ ,

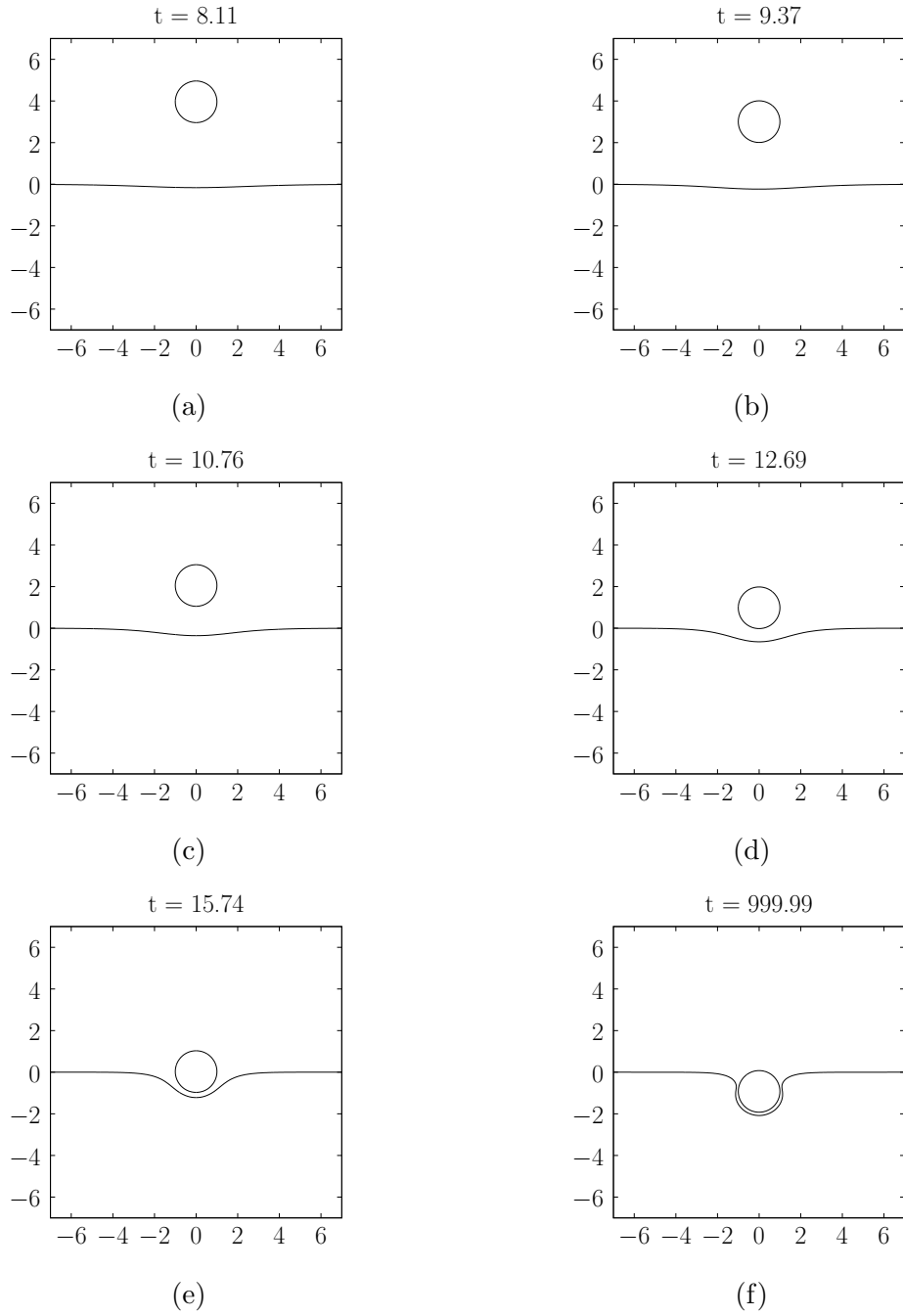


Figure 15: Settling of a sphere onto the interface when  $D = 2.2$ ,  $Bo = 2.5$  and  $\lambda = 1$ . The interface deforms as the sphere approaches and the sphere attains an equilibrium position with a thin film of fluid trapped between the sphere and the interface.

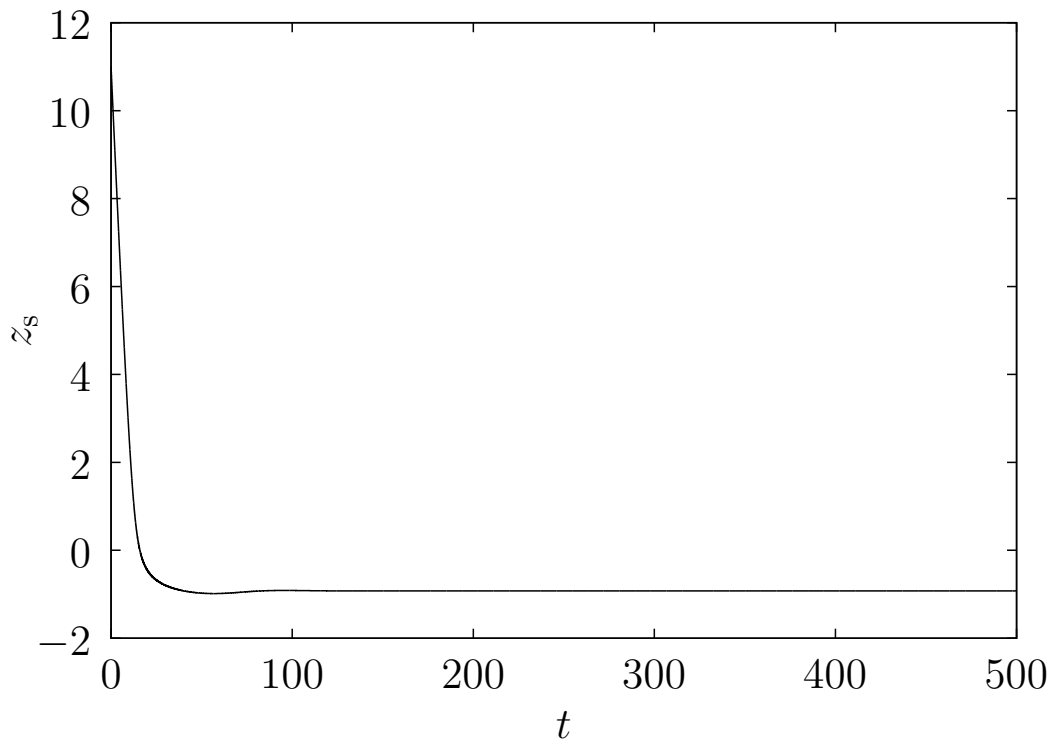


Figure 16: Position curve of the sphere, which is seen to attain an equilibrium position at the interface.

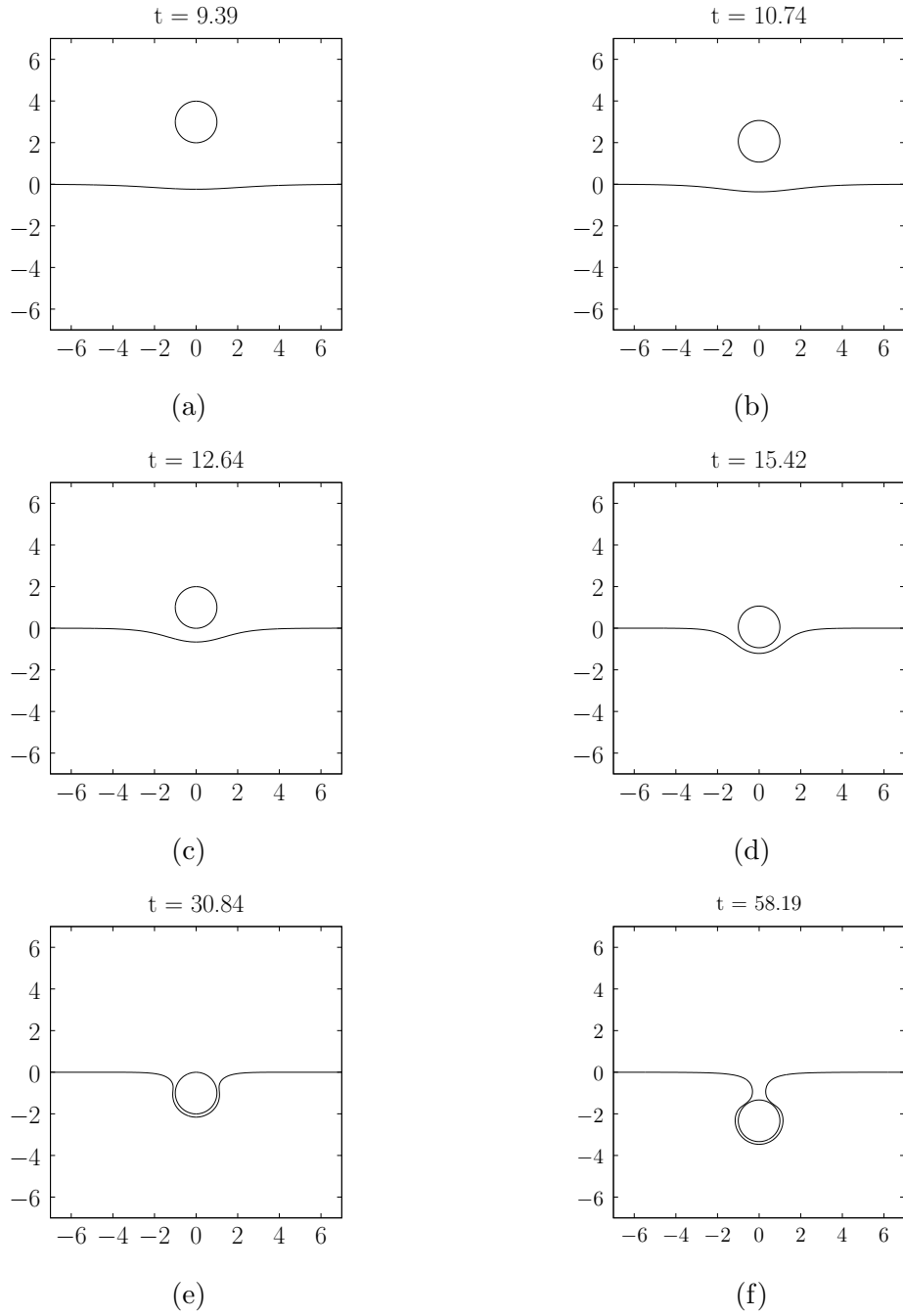


Figure 17: Settling of a sphere onto and through the interface when  $D = 2.2$ ,  $Bo = 3.5$  and  $\lambda = 1$ . The interface deforms as the sphere approaches and envelopes the sphere as it sinks.

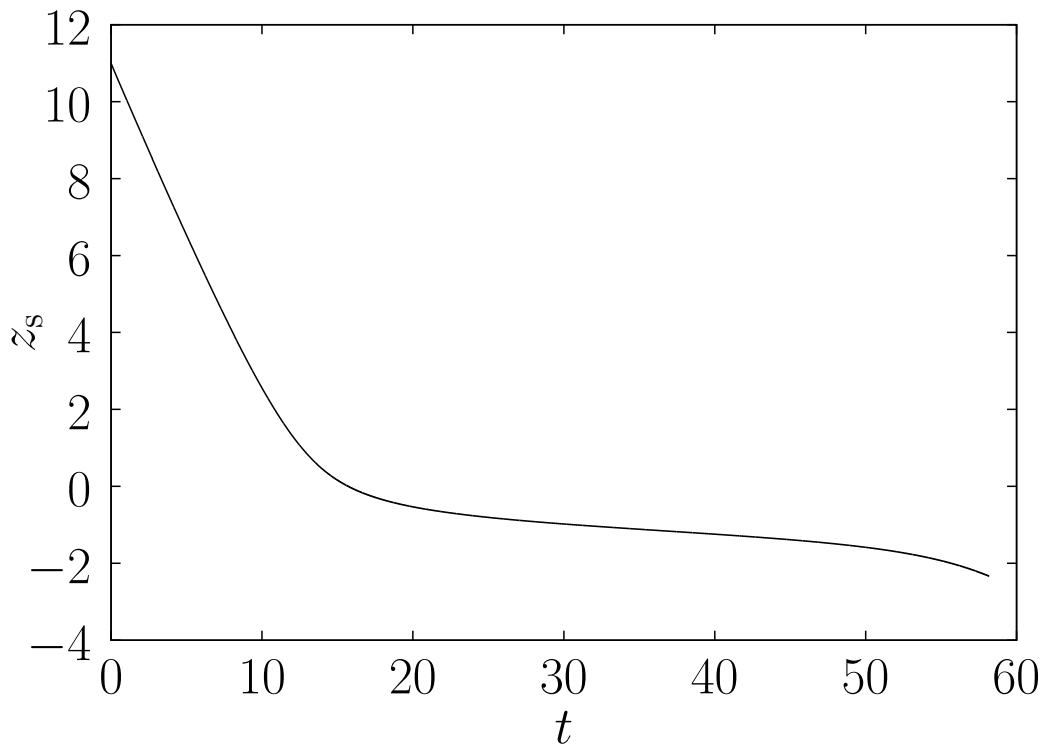


Figure 18: Position curve of the sphere, which is seen to slow down at the interface, before accelerating away.

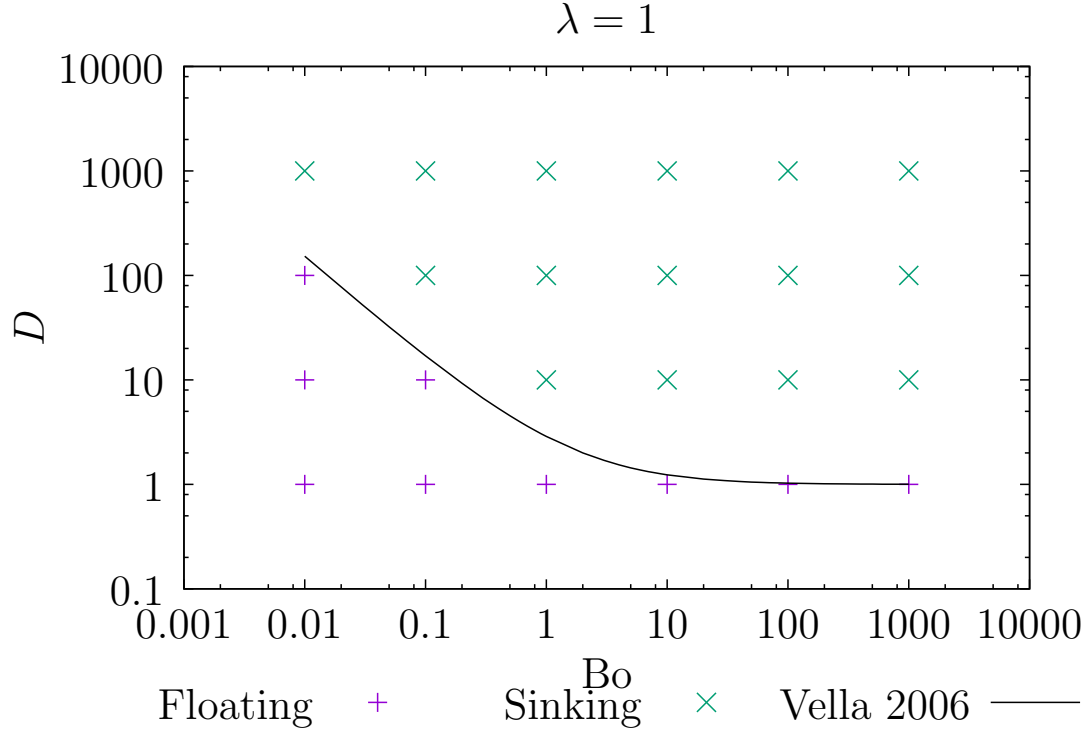


Figure 19: A regime diagram showing the fields of floating and sinking in the  $\lambda = 1$  plane of the parameters space defined by  $\lambda, Bo, D$ . Points show results of simulations. Solid line shows prediction from theoretical model of (Vella et al., 2006).

$Bo$  and  $\lambda$  is independent of  $\lambda$ . Figure 19 shows the transition in a plane of constant  $\lambda$  over orders of magnitude variation in  $D$  and  $Bo$ . Also shown is the prediction for this transition from the theoretical model of (Vella et al., 2006). This model finds the maximum  $D$  for a given  $Bo$  and contact angle for a sphere to be at equilibrium at an interface. This is different from our model, since no initial motion of the sphere is considered, and the existence of a contact line on the sphere is imposed. Despite these differences, we see that the results in figure 19 agree with this model. In figure 20 however, we show the results of a denser investigation of the parameter space, in the region where the transition curve has the highest curvature. It can be seen that although our model reproduces the shape of the predicted regime boundary, there is an offset such that our model predicts a higher maximum value of  $D$  for a given  $Bo$ .

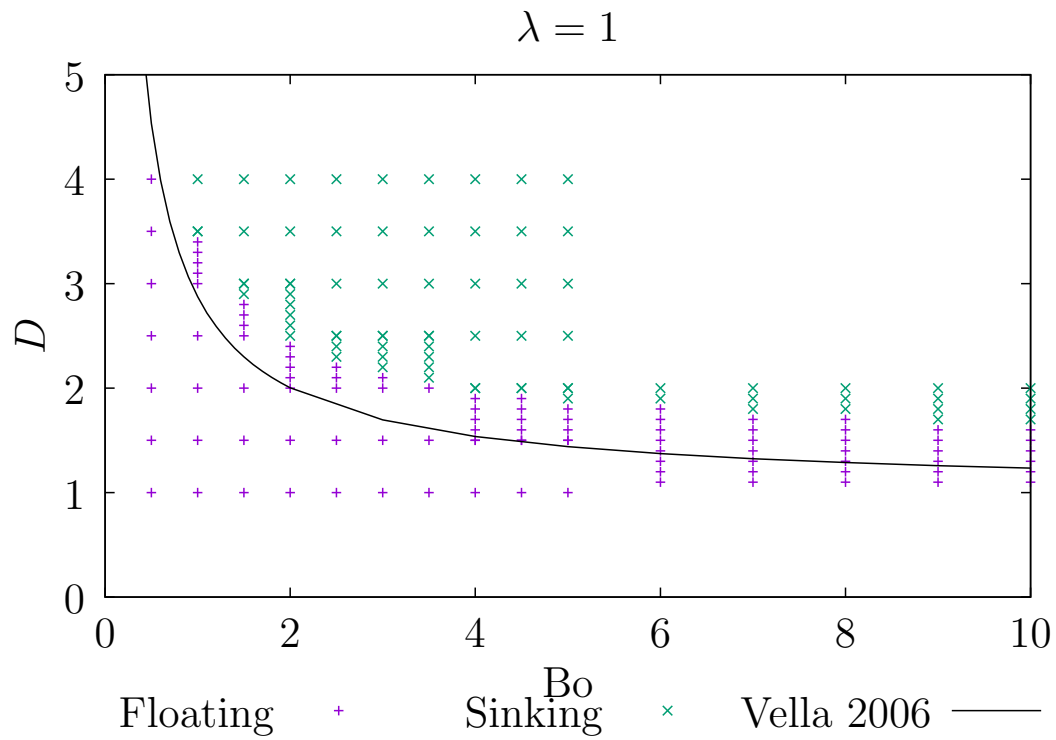


Figure 20: A regime diagram showing the fields of floating and sinking in the  $\lambda = 1$  plane of the parameters space defined by  $\lambda, Bo, D$ . Points show results of simulations. Solid line shows prediction from theoretical model of (Vella et al., 2006).

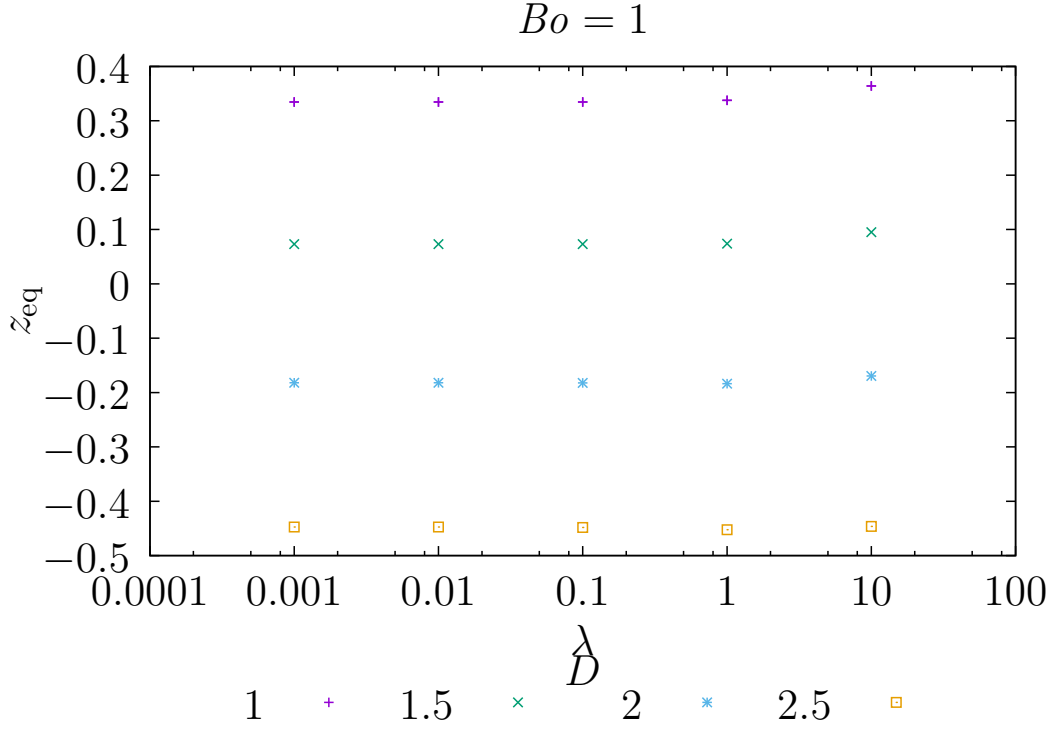


Figure 21: Plots of  $z_{\text{eq}}$  versus  $\lambda$  for  $Bo = 1$  and different values of  $D$ . It is seen that there is no dependence on  $\lambda$ . The same is true for other values of  $Bo$ .

### 6.1.2 Equilibrium Floating Position

For simulations where the sphere is observed to attain a static equilibrium position, the dependence of the final height of the sphere  $z_{\text{eq}}$  on  $D$ ,  $Bo$  and  $\lambda$  has been determined. A key result is that  $z_{\text{eq}}$  is independent of the viscosity ratio as seen in figure 21. Figure 22 shows the dependence of  $z_{\text{eq}}$  on  $Bo$  for different values of  $D$ . There are a number of points to note here. Firstly, as  $Bo \rightarrow 0$ , the dependence of  $z_{\text{eq}}$  on  $D$  vanishes, and  $z_c \rightarrow 0$ . Once  $Bo > 0.01$ ,  $z_c$  decreases and the equilibrium position of sphere is deeper with respect to the plane of the undeformed interface. For a given  $Bo$ , the larger the value of  $D$ , the deeper the equilibrium position of the sphere. For  $D \neq 1$ , as  $Bo$  increases the floating-sinking transition is crossed and  $z_{\text{eq}} \rightarrow -\infty$ . For  $D = 1$ , as  $Bo \rightarrow \infty$ ,  $z_c \rightarrow -0.32$ .



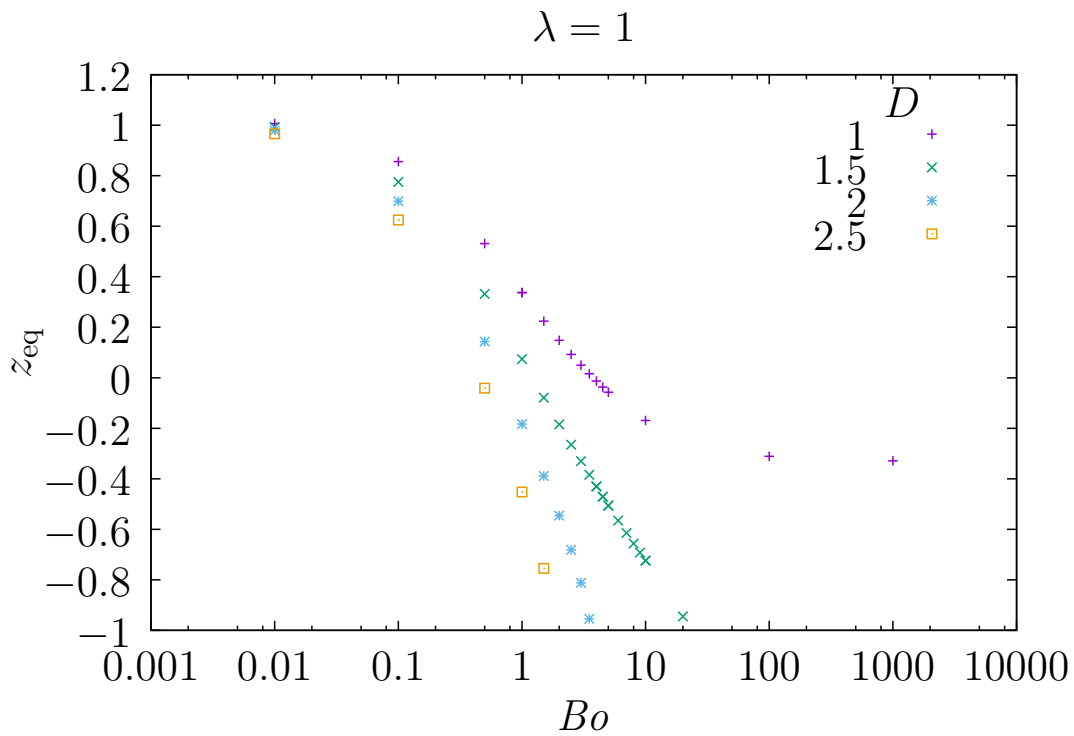


Figure 22: Plots of  $z_{\text{eq}}$  versus  $Bo$  for  $\lambda = 1$  and different values of  $D$ . As  $Bo \rightarrow 0$ ,  $z_{\text{eq}}$  becomes independent of  $D$ . As  $Bo$  increases, the sphere transitions to sinking and so the plots cannot be continued to higher  $Bo$ .

### 6.1.3 Entrained Volume

As described in section 4, one of the criteria for the termination of the model is that two separate branches of the interface become closer to each other than the smallest interval length on either the sphere or the interface. In the case, the interface is assumed to snap at this point and the volume of upper phase fluid beneath the point of snapping is defined as the entrained volume  $V$ . The range of parameters for which the entrained volume was investigated is limited by the termination criteria of the model. For  $D < 4$  or  $\lambda > 0.03$ , most simulations where sinking was observed terminated when the sphere and the interface became too close. For  $D = 4$ , the same is true for  $Bo < 1$  and as  $D$  increases, this critical value of  $Bo$  decreases, such that for  $D = 1000$  interface snapping was observed down to  $Bo = 0.01$ , the smallest value used.

Figure 23 shows the dependence of the entrained volume of  $Bo$  for different values of  $D$  and  $\lambda$ . For  $D = 8$  (figure 23a), it can be seen that for  $Bo < 1$ ,  $V$  is approximately independent of  $\lambda$  and  $V \sim \ln Bo$ . For  $Bo > 1$ ,  $V$  becomes independent of  $Bo$  and there is a weak dependence on  $\lambda$ ; the more viscous the upper fluid relative to the lower fluid, the greater the volume of entrained fluid. Increasing  $D$  to 50 (figure 23b) it can be seen that the viscosity independent linear relationship between  $V$  and  $\ln Bo$  is present for  $\ln Bo < -2$  ( $Bo < 0.14$ ). For larger Bond numbers,  $V$  again becomes independent of  $Bo$  although the viscosity dependence is stronger than for  $D = 8$ . Additionally, for a given  $Bo$  and  $\lambda$ ,  $V$  is greater for  $D = 50$  than  $D = 8$ .

These trends are continued to higher values of  $D$  (figures 23c and 23d). The transitional value of  $Bo$  decreases as  $D$  increases; for  $D = 1000$  this transitional value is smaller than the smallest  $Bo$  used. Also, as  $D$  increases at fixed  $\lambda$  and  $Bo$ , so does  $V$ .

Figure 24 shows the same data as in figure 23 but with curves with different values of  $D$  shown on the same plot with a fixed value of  $\lambda$ . All of the previously described features can be observed including the two regimes:  $V \sim \ln Bo$  and  $V \neq V(Bo)$ , and the increase in  $V$  with increasing  $D$  and decreasing  $\lambda$ .

In magmas, the IFt  $\sigma$  between two melts is expected to be equal to zero or very small

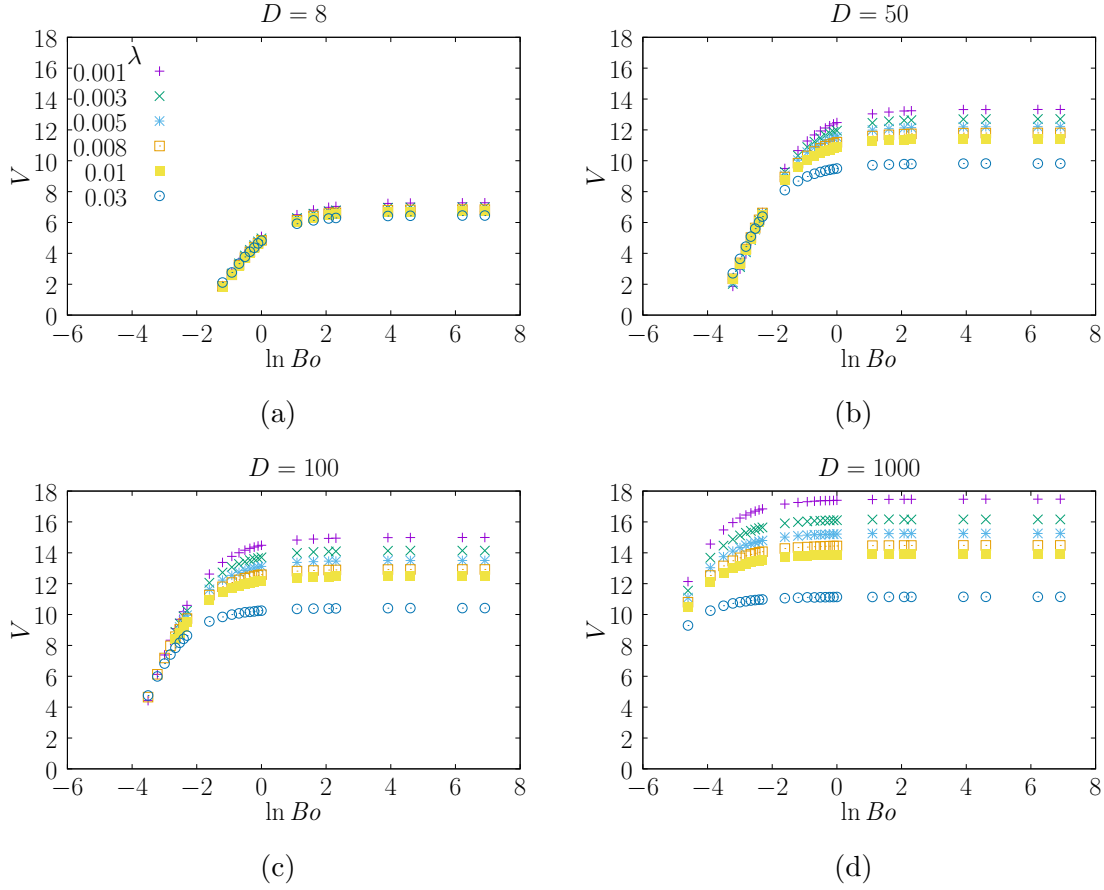


Figure 23: Dependence of entrained volume  $V$  on  $Bo$  for different  $\lambda$  for a)  $D = 8$ , b)  $D = 50$ , c)  $D = 100$  and d)  $D = 1000$ . At small  $Bo$  there seems to be a linear relationship between  $V$  and  $\ln Bo$  but as  $Bo$  increases,  $V$  becomes independent of  $Bo$ .

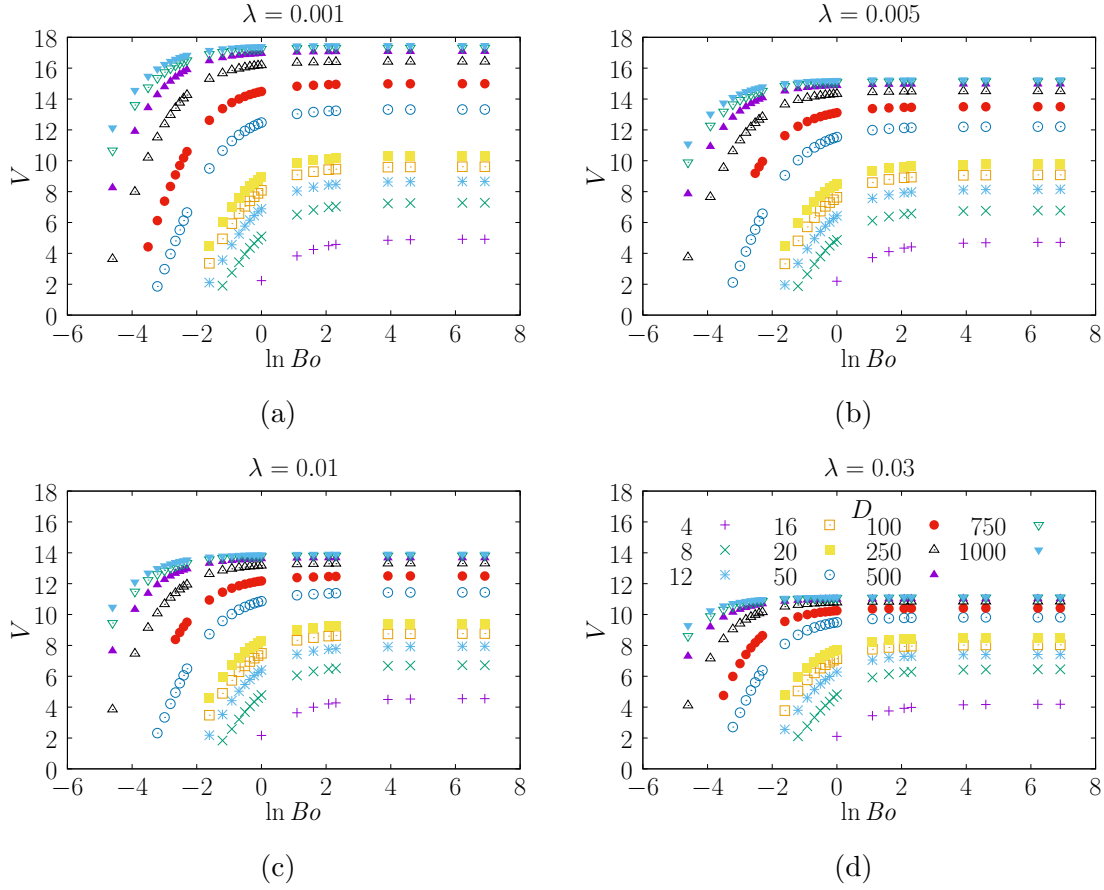


Figure 24: Dependence of entrained volume  $V$  on  $Bo$  for different  $D$  for a)  $\lambda = 0.001$ , b)  $\lambda = 0.005$ , c)  $\lambda = 0.01$  and d)  $\lambda = 0.03$ . At small  $Bo$  there seems to be a linear relationship between  $V$  and  $\ln Bo$  but as  $Bo$  increases,  $V$  becomes independent of  $Bo$ .

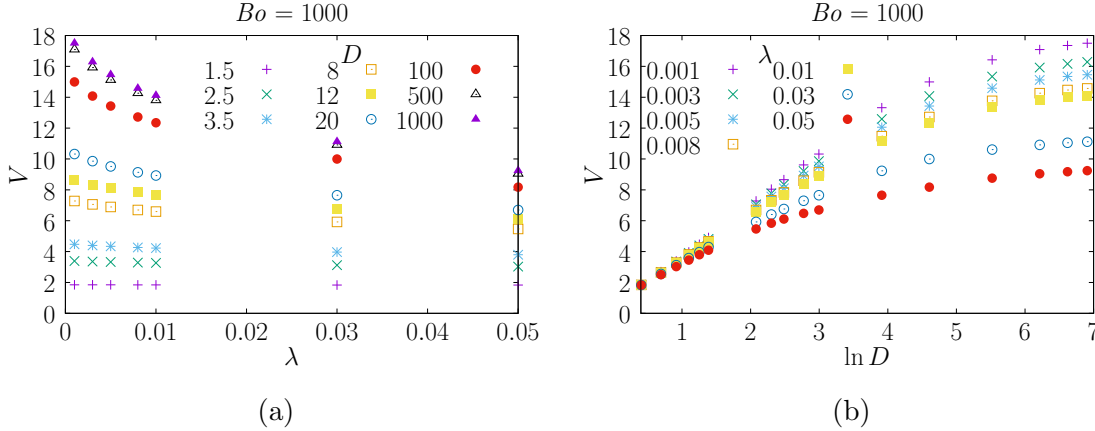


Figure 25: Dependence of  $V$  on a)  $\lambda$  for different  $D$  and b)  $D$  for different  $\lambda$ , for  $Bo = 1000$ , which is in the regime where  $V$  is independent of  $Bo$ .

(melts of different compositions are miscible). Therefore, in magmatic systems  $Bo \rightarrow \infty$ . Motivated by this, figure 25 shows the dependence of  $V$  on  $\lambda$  and  $D$  for  $Bo = 1000$ , which as can be seen from figures 23 and 24 is well into the regime where  $V$  is independent of  $Bo$ . Hence, these results can be considered the same as for when  $Bo \rightarrow \infty$ . As seen in figure 25a, for small values of  $D$  ( $\leq 3.5$ )  $V$  is nearly independent of  $\lambda$ . However, as  $D$  increases, it is seen that  $V$  decreases with  $\lambda$ . These features can also be seen in figure 25b where it appears that the dependence on  $D$  can be split into two regimes. For  $\ln D$  between 0 and some critical value,  $V \sim \ln D$ . For  $\lambda = 0.001$ , this critical value is approximately 3, and this decreases to 1.4 for  $\lambda = 0.05$ . Above this critical value, the dependence on  $D$  weakens, and it is possible that as  $D \rightarrow \infty$ ,  $V$  becomes independent of  $D$ , although further simulations at higher  $D$  would be needed to verify this.

#### 6.1.4 Sinking Timescale

The sinking timescale  $t_s$  is defined as the time between the sphere first touching the plane of the undeformed interface and the moment at which the sphere loses contact with the bulk of the upper phase i.e. when the tail snaps. Within the BIM, this is interpreted as the moment at which the separation between the two branches of the interface becomes smaller than the separation between the points used to discretise it. Figure 26 shows the

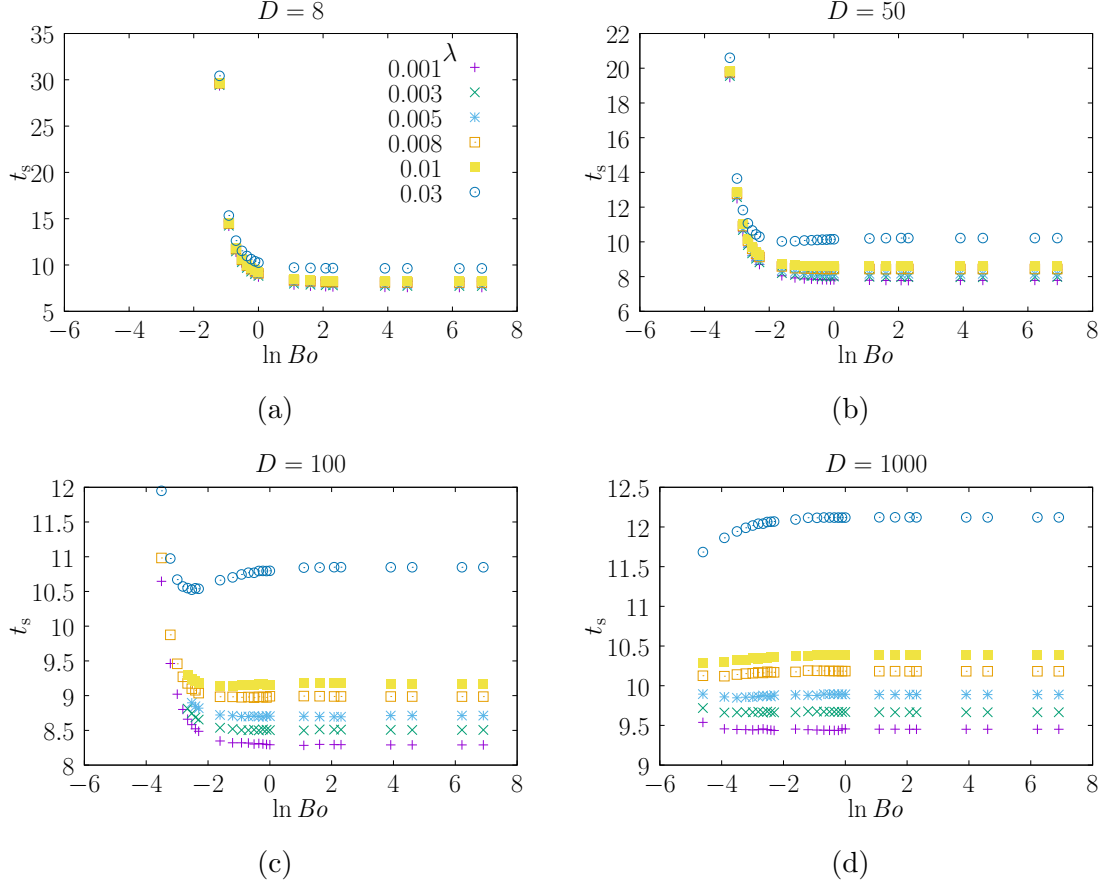


Figure 26: Dependence of the sinking timescale  $t_s$  on  $Bo$  for different  $\lambda$  and a)  $D = 8$ , b)  $D = 50$ , c)  $D = 100$  and d)  $D = 1000$ . Note the difference in vertical scale between the figures.

dependence of the sinking time on the Bond number, for different values of the MDR and viscosity ratio. It is observed that the function  $t_s = t_s(Bo, D, \lambda)$  is not simple. For all values of  $D$  and  $Bo$ , the larger the value of the viscosity ratio, the longer the sinking time. Additionally, for all values of  $D$ , as  $Bo$  approaches the floating transition, the time taken for sinking tends to infinity, and as  $Bo \rightarrow \infty$  the sinking time becomes independent of  $Bo$ . However, the behaviour is complicated for intermediate value of  $Bo$ . For  $D = 8$ , the decrease in sinking time with  $Bo$  is monotonic. However as  $D$  increases, a minimum in the sinking time as a function of  $Bo$  appears. This minimum only appears for larger values of the viscosity ratio and becomes more pronounced as the viscosity ratio increases. For the case  $D = 1000$ , it is inferred that the minimum in the curve for  $\lambda = 0.03$  occurs at a value of  $Bo < 0.01$  (the smallest Bond number investigated).

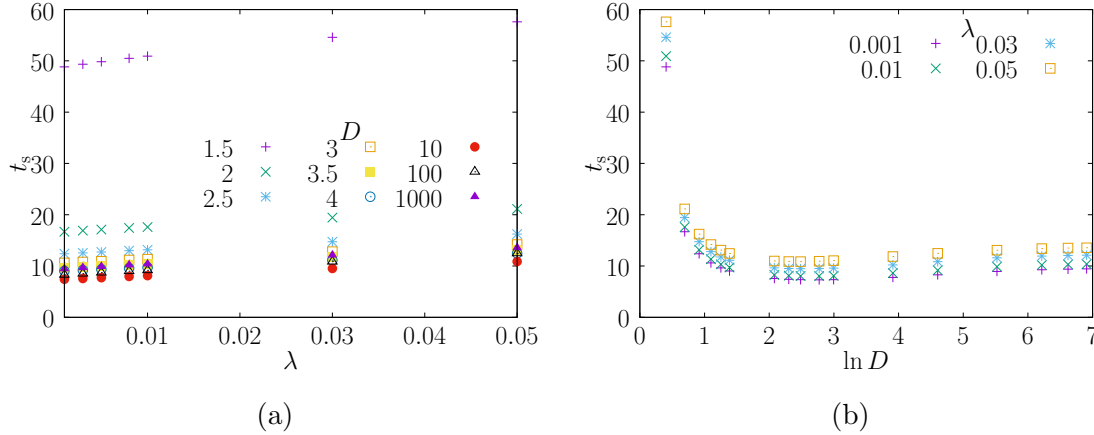


Figure 27: Dependence of  $t_s$  on a)  $\lambda$  for different  $D$  and b)  $D$  for different  $\lambda$ , for  $Bo = 1000$ , which is in the regime where  $t_s$  is independent of  $Bo$ .

Bearing in mind the application to mixing magmas, the high Bond number limit has been investigated (figure 27). As before, figure 27a shows that an increase in the value of the viscosity ratio leads to an increase in the sinking timescale. Like with  $Bo$ , the sinking timescale depends on  $D$  in a non-monotonic fashion (figure 27b). As  $D \rightarrow 1$ ,  $t_s \rightarrow \infty$  and as  $D \rightarrow \infty$  the sinking timescale becomes independent of  $D$ . However, there is a local minimum in the value of  $t_s$  at approximately  $\ln D \approx 2$  ( $D \approx 7.3$ ).

## 6.2 Settling Spheroids

The settling of non-spherical particles shows different behaviour. Figure 28 shows the settling of an oblate spheroid of aspect ratio  $R = 0.5$  onto an interface, where the dimensionless parameters are  $D = 2$ ,  $Bo = 10$  and  $\lambda = 1$ . As can be seen, the spheroid is able to float at the interface. Comparing with figure ?? it can be seen that for these values, spheres are observed to sink through the interface. Therefore, decreasing the aspect ratio of the particle can inhibit sinking.

Figure 29 compares the sinking of a sphere and that of a spheroid of aspect ratio 0.5 where  $D = Bo = 1000$  and  $\lambda = 1$ . It is seen that at a given depth, the interfacial profile in both simulations is very similar, although it takes the spheroid much longer for it to reach that depth. In all simulations of an oblate spheroid where sinking was observed, all

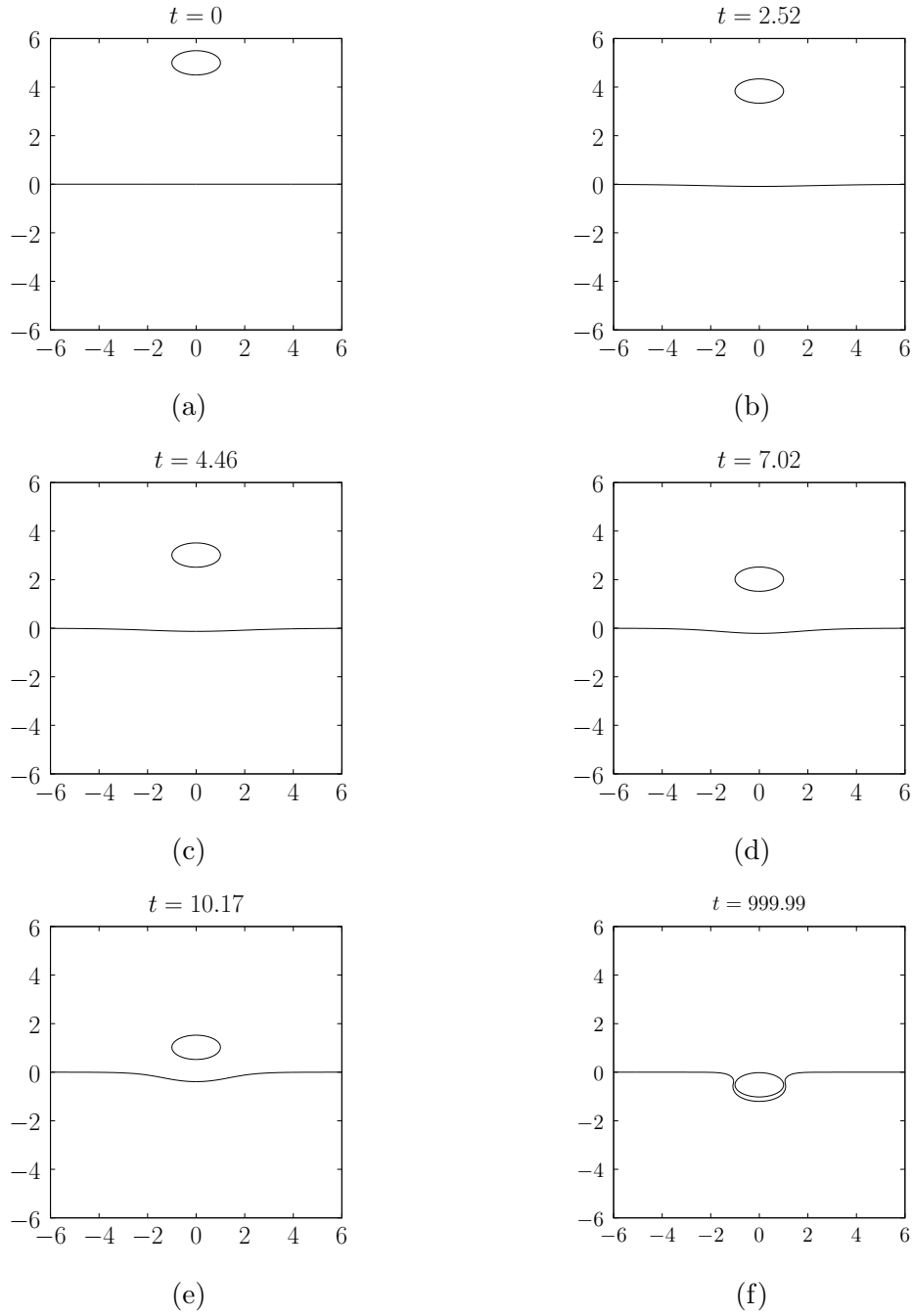


Figure 28: Settling of an oblate spheroid with aspect ratio  $R = 0.5$  onto the interface when  $D = 2$ ,  $Bo = 10$  and  $\lambda = 1$ . The interface deforms as the sphere approaches and forms a depression into which the spheroid sits.



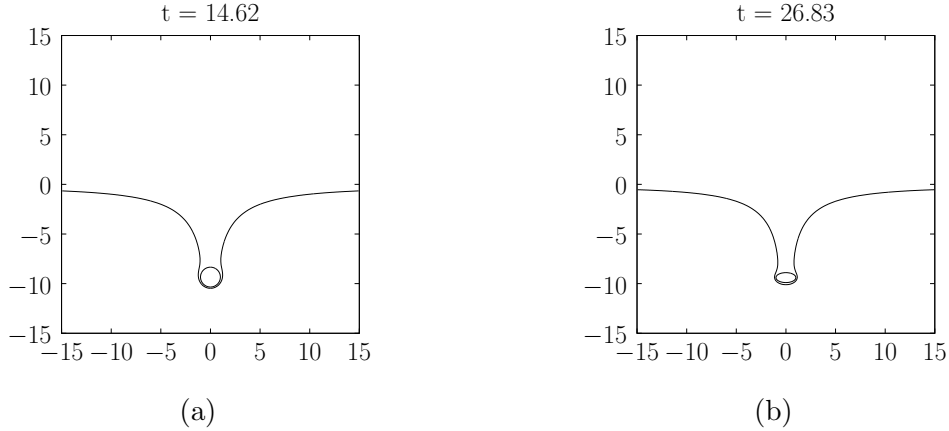


Figure 29: Comparing the sinking of a a) sphere and an b) oblate spheroid with  $R = 0.5$  for  $D = Bo = 1000$  and  $\lambda = 1$ . Both interfacial profiles are very similar.

models terminated due to the separation between particle and interface becoming smaller than the distance between discretisation points. Hence, no simulations proceeded to tail snapping and therefore no data has been obtained regarding the sinking timescale and the entrained volume.

## 7 Discussion

### 7.1 Floating versus Sinking

Figure 20 shows the location of the floating and sinking regimes in the parameter space defined by  $Bo$  and  $D$ , as found using the BIM presented in sections 3 and 4. The curve in the figure shows the prediction for the transition between the two regimes found from the model of Vella et al. (2006) for a contact angle of  $\pi$  (sphere is completely wetted by upper fluid). It can be seen that for a given  $Bo$ , the transition predicted by the BIM is found at a higher value of  $D$  than for the model presented by Vella et al. (2006). To rationalise this discrepancy, a brief description of the Vella et al. (2006) model is given here, highlighting the key differences with the BIM. Motivated by these differences, modifications are then proposed to the Vella et al. (2006) model and the validity of these is determined by

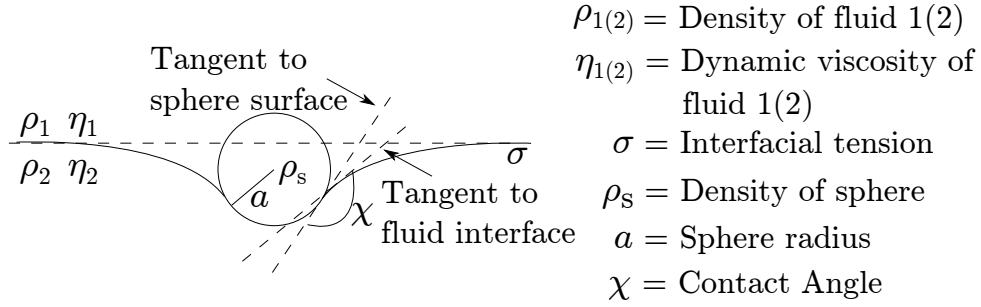


Figure 30: The configuration of the problem as modelled by Vella et al. (2006). The key difference between this and the BIM presented in sections 3 and 4 is that this model is static, and a three phase contact line is assumed.

comparing with the results from the BIM.

#### 7.1.1 Vella et al. (2006) Model: A static description of the floating - sinking transition

The model proposed in Vella et al. (2006) considers the static problem of a sphere sitting at the interface between two immiscible, density stratified fluids. The presence of a three-phase contact line is assumed. The configuration is as seen in figure 30. The model is a force balance of the surface tension, buoyancy and gravitational forces present in the system, and finds the condition for there to be an equilibrium position of the sphere at the interface.

In order to construct this model, it is necessary to consider a result from Keller (1998); the vertical contribution of the IFT force on an object floating at an interface is equivalent to the buoyancy force of the fluid in the meniscus. This was first hypothesised by Galilei (Galilei, 1663; Vella, 2007). Figure 31 is a useful aid in explaining this. The volume of the meniscus is shown by the shaded regions external to the vertical cylindrical surface which contains the contact line. The IFT contribution to the vertical force is equal to the buoyancy of the upper fluid in this region. This means the force balance for a sphere in

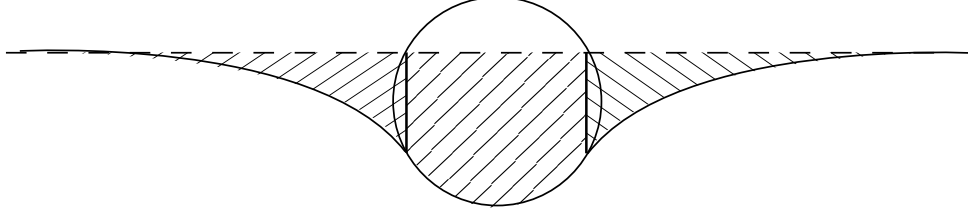


Figure 31: The different shadings show the regions internal and external to the meniscus.

equilibrium can be expressed as

$$\frac{4\pi(\rho_s - \rho_1)a^3g}{3} = 2\pi a\sigma \sin \theta_c \sin(\chi - \theta_c) + (\rho_2 - \rho_1)g \left( \frac{\pi a^3(2 + 3 \cos \theta_c - \cos^3 \theta_c)}{3} - \pi z_c a^2 \sin^2 \theta_c \right) \quad (80)$$

where  $\theta_c$  and  $z_c$  are the polar and vertical coordinates of the contact line respectively. The left hand side corresponds to the weight of the sphere relative to the weight of the same volume of the upper fluid. The right hand side is the sum of the IFT contribution (equivalent to the buoyant force due to the volume of the meniscus external to the contact line), and the displaced weight of the lower fluid relative to the upper fluid, in the volume of the meniscus internal to the contact line (central shaded region in figure 31).

Using the non-dimensionalisation scheme presented in section 3.1 the force balance can be written as

$$D = \frac{3 \sin \theta_c \sin(\chi - \theta_c)}{2Bo} + \frac{2 + 3 \cos \theta_c - \cos^3 \theta_c}{3} - \frac{3z'_c \sin^2 \theta_c}{4} \quad (81)$$

For a given  $Bo$ , contact angle  $\chi$  and contact line position (given by  $\theta_c$  and  $z'_c$ ), this equation gives the largest possible value of  $D$  for which an equilibrium floating position exists. The contact line position itself is found by solving the Laplace-Young equation

for the interfacial profile subject to the boundary condition given by the contact angle condition on the sphere, and imposing that the interface returns to its equilibrium position away from the sphere. This is a boundary value problem (Riley et al., 2006) and has no analytical solution in an axisymmetric geometry so needs to be solved numerically.

Hence, the routine for finding the maximum  $D$  at which floating can occur for a given  $Bo$  and  $\chi$  is found by sweeping over different values of  $\theta_c$  between 0 and  $\pi$  and solving the Laplace-Young equation for the corresponding height of the contact line  $z_c$  for each case. These are then substituted into equation 81. The largest value of  $D$  calculated in the sweep is the largest value of  $D$  for which floating is possible for a given  $Bo$  and  $\chi$ . The curve shown in figure 20 is the predicted floating-sinking transition for  $\chi = \pi$ .

### 7.1.2 Difference between the static and BIM models

To explain the discrepancy between the two models in their prediction of the floating-sinking transition location in the  $Bo$ - $D$  parameters space, it is important to consider the differences between the models. The static model, as suggested by its name, is static. It merely considers the conditions at which a sphere can be in equilibrium at an interface, given a contact line exists. It doesn't account for any prior motion of the sphere. It has been shown for cylinders and a liquid-gas interface that increasing the speed of impact reduces the maximum density and/or size of cylinder that can float at the interface Vella and Metcalfe (2007); Vella and Li (2010). This situation is theoretically considered by using an initial condition of the cylinder being in contact with the interface but having some initial velocity. It is important to note that in these studies the flow is in the inertial regime.

The key difference with the BIM used in this study is that in the initial state of the system the sphere is multiple radii above the interface and is settling at its terminal velocity. Hence, as well as having an initial velocity, no contact line exists. Since there is a no-slip boundary condition on the surface of the sphere (equation 50), the fluid immediately adjacent to the sphere will never be displaced. This means that there will

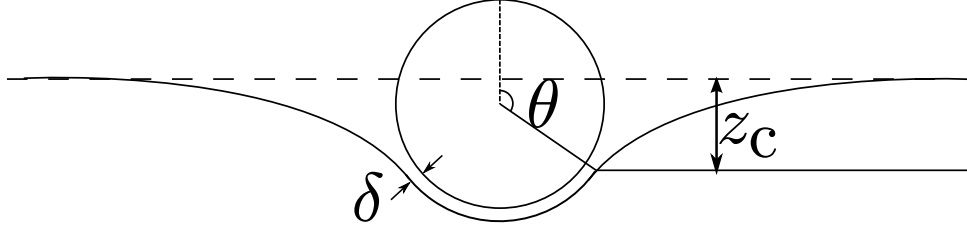


Figure 32: The modified static model configuration. The sphere and the interface are separated by a film of upper phase fluid of constant thickness  $\delta$ .

always remain a layer of upper phase fluid between the sphere and the interface. Hence it is impossible to reproduce the film drainage mode as seen in the experimental study. The presence of this layer will also have an effect on the floating-sinking transition, since it is effectively provides an extra contribution to the upward buoyancy forces.

For a given  $Bo$ , the BIM predicts the value of  $D$  at which the floating-sinking transition occurs to be positively displaced relative to the prediction from the static model. This suggests that the effect of the trapped layer of upper phase fluid between the sphere and the interface has a more significant effect than the impact of the sphere.

### 7.1.3 Modified static model

Motivated by the observation that the trapped layer has a greater effect on the floating-sinking transition than the impact of the sphere, a static model, modified from that described in section 7.1.1, is presented here which accounts for a trapped layer of upper phase fluid (figure 32). For simplicity, this layer is assumed to have a uniform thickness. Hence, in this model, the interface can be described by two parts. The first is a spherical cap of radius  $a + \delta$  concentric with the sphere. At some polar angle  $\theta_c$  this transitions into a meniscus whose geometry is determined by the Laplace-Young equation subject to the condition that at  $\theta = \theta_c$ , the tangent planes to both the spherical cap and the meniscus are coincident.

The force balance for this geometry can be realised by modifying equation 80 by replacing

all the occurrences of  $a$  on the right-hand side by  $a + \delta$  and setting  $\chi = \pi$ ;

$$\frac{4\pi(\rho_s - \rho_1)a^3g}{3} = 2\pi(a+\delta)\sigma \sin^2 \theta_c + (\rho_2 - \rho_1)g \left( \frac{\pi(a+\delta)^3(2 + 3\cos \theta_c - \cos^3 \theta_c)}{3} - \pi z_c(a+\delta)^2 \sin^2 \theta_c \right). \quad (82)$$

As in section 7.1.1, this can be non dimensionalised to give

$$D = \Delta^{1/2} \left( \frac{3 \sin^2 \theta_c}{2Bo} + \frac{\Delta(2 + 3\cos \theta_c - \cos^3 \theta_c)}{4} - \frac{3z'_c \Delta^{1/2} \sin^2 \theta_c}{4} \right) \quad (83)$$

where

$$\Delta = \left( 1 + \frac{\delta}{a} \right)^2. \quad (84)$$

For a given  $Bo$ ,  $\theta_c$  and  $\Delta$ , equation 83 gives the maximum value of  $D$  for which a sphere is in equilibrium whilst separated from an interface by a film of thickness  $\delta$ . Using a routine similar to that described in section 7.1.1 the floating-sinking transition in the  $Bo$ - $D$  space for different  $\delta$  can be found (figure 33). It can be seen that increasing the value of  $\Delta$ , and so the relative thickness of the trapped film, it is possible to support denser and larger spheres at a fluid interface. This is intuitively explained by the additional contribution of the buoyant fluid in the film to the upward force.

#### 7.1.4 Comparison with BIM results

To test if the modified static model provides a suitable explanation for the observed floating-sinking transition in the BIM results, the results of four simulations where floating was observed but the parameters are close to the transition were chosen for further analysis (see table 2). For each of these simulations, the final profile of the thickness of the film separating the sphere from the interface was considered (figure 34) and the mean thickness of the film, weighted by the radial coordinate of the fluid, was calculated (given in table 2).

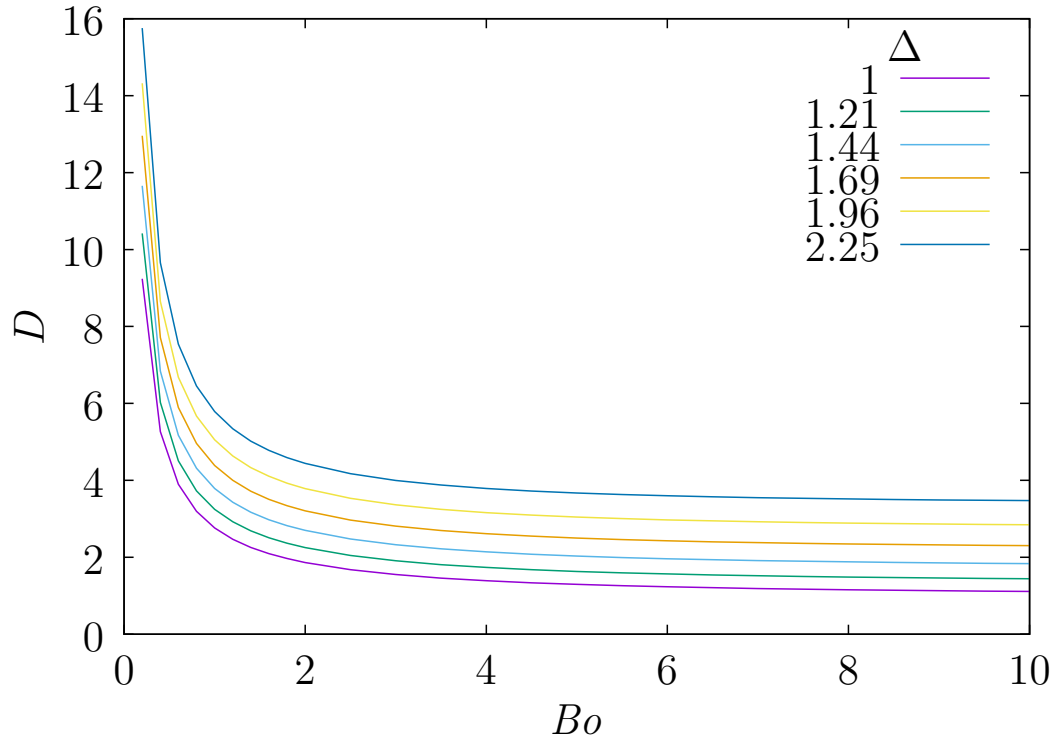


Figure 33: Plots of equation 83 for different values of  $\Delta$ . As  $\Delta$  increases the floating-sinking transition at a given value of  $Bo$  shifts to higher values of  $D$ .

Table 2: BIM simulations chosen for comparison with the modified static model, and the mean final thickness of the film separating the sphere from the interface.

$D$	$Bo$	$\bar{\delta}$	$\Delta$
3.4	1.0	0.175	1.381
2.8	1.5	0.171	1.371
2.2	2.5	0.160	1.346
2.0	3.5	0.157	1.339

As can be seen in figures 35a to 35d, the film is seen to contract at its periphery. This agrees with previous experimental observations (Hartland, 1968) where it has been noted that the film constricts at it's periphery, just inside the point where it transitions to the meniscus profile. This constriction is predicted by the theoretical model of (Jones and Wilson, 1978) as a consequence of pressure gradients in the film as a consequence of the change in curvature of the interface at the film periphery.

Additionally, the point where the film transitions to the meniscus occurs at a polar angle of  $\theta \approx \pi/2$ . This is the first point of agreement with the modified static model. Differentiating of equation 83 with respect to  $\theta_c$  and setting  $\partial D/\partial\theta_c = 0$  gives a solution of  $\theta_c = \pi/2$  (other solutions may exist but cannot be extracted due to the unavailability for a closed expression for  $\partial z_c/\partial\theta_c$ ). Hence, there is a (at least a local) maximum in maximum value of  $D$  for which floating can occur at  $\theta_c = \pi/2$ . Since the chosen simulations are close to the transition, it is to be expected that they have an equilibrium configuration which gives this maximum upward force.

Figure 34e shows the film thickness as a function of  $\theta$  for the different simulations. It can be seen that, unlike in the modified static model, the film has a variable thickness which can vary by up to 50%. Therefore, to compare these simulations with the results from the static model, the mean thickness of the film, weighted by the radial coordinate, has been calculated. The reason for weighting by the radial coordinate is because the axisymmetric geometry means, for a given film thickness, there is a greater volume of fluid at a larger radius. The weighted mean thicknesses  $\bar{\delta}$  and their corresponding value of  $\Delta$  are given



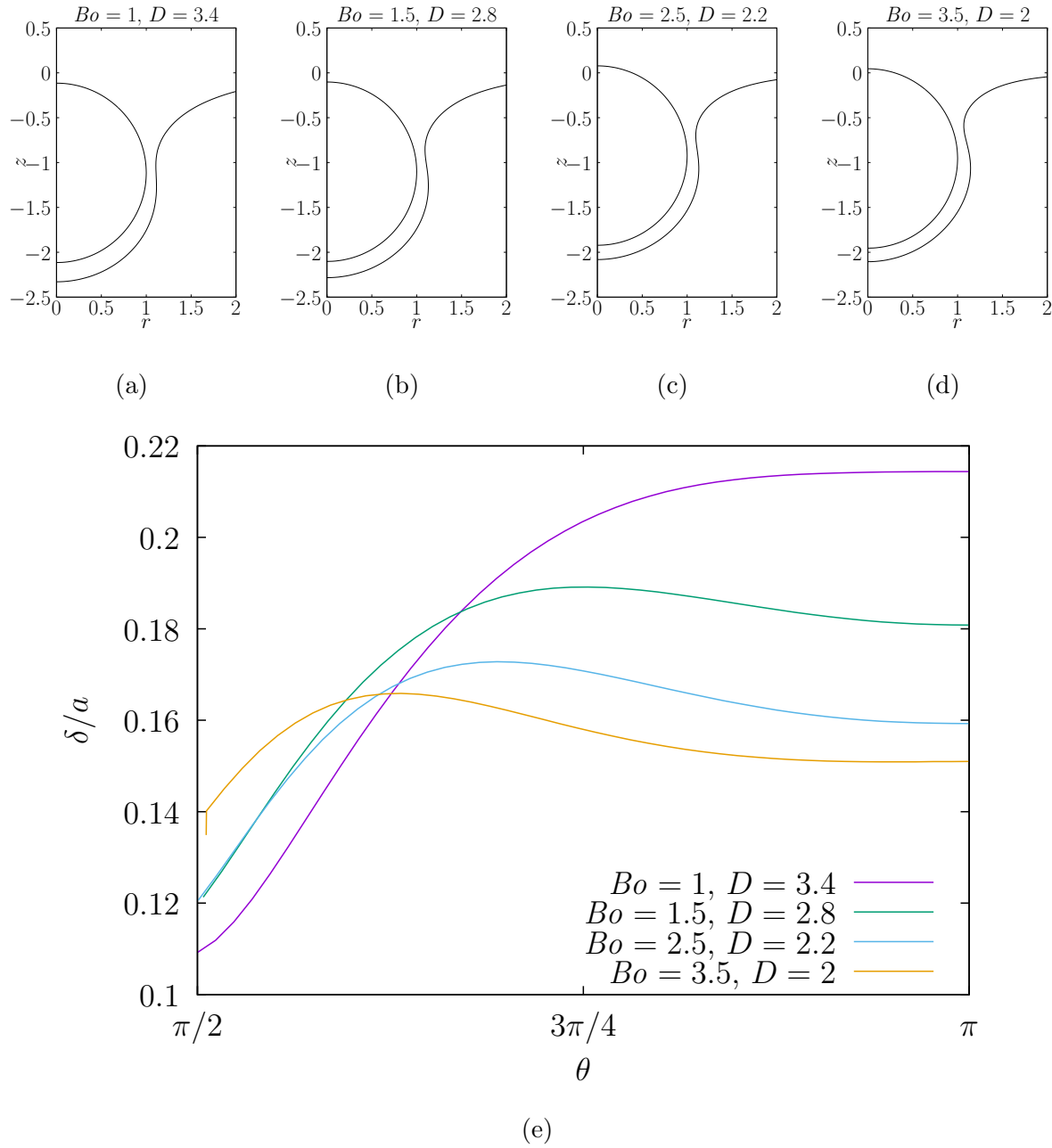


Figure 34: a) to d) The final equilibrium configuration of the simulations listed in table 2. In each example, the film constricts at approximately  $\theta = \pi/2$ , just before the interface transitions into the meniscus profile. e) Film thickness as a function of  $\theta$ . The film thickness can be seen to vary up to about 50%.

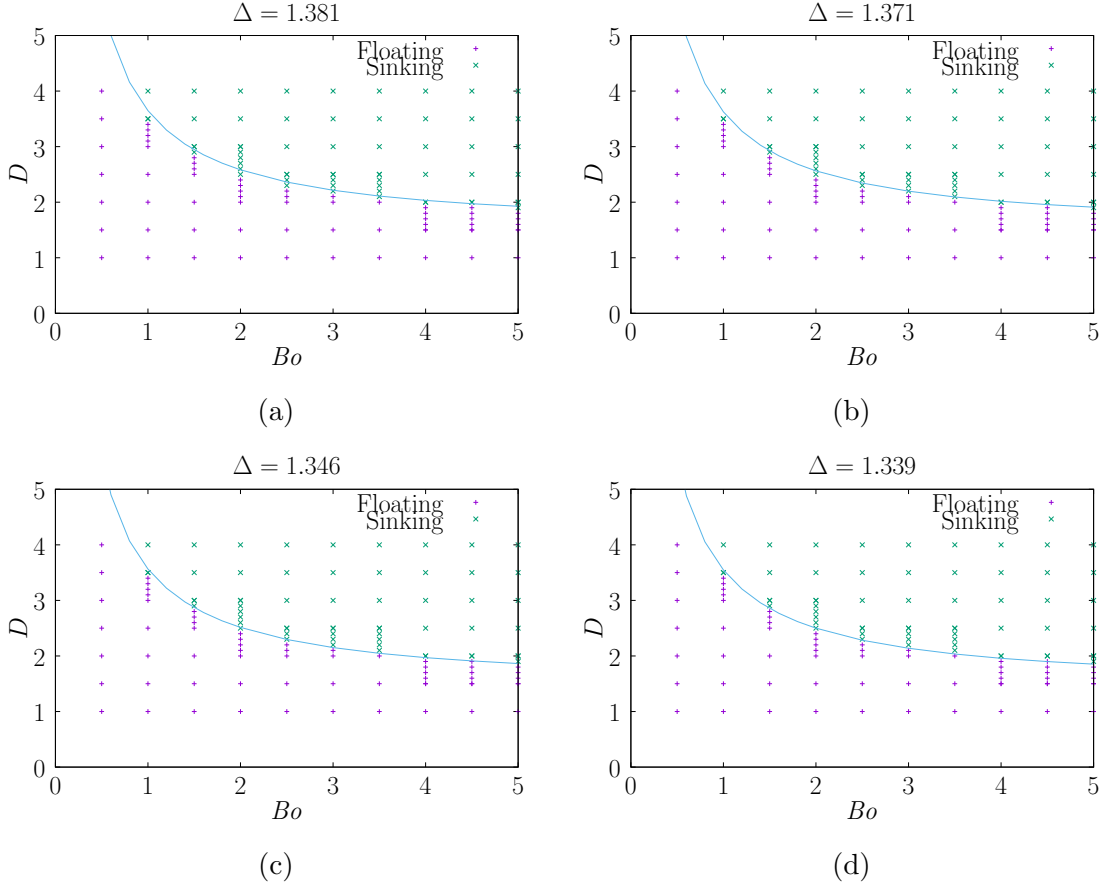


Figure 35: Predicted transitions based on the mean thickness of each film.

in table 2. Figure 35 shows the predicted transitions for these values of  $\Delta$  compared to the results from the BIM. It can be seen that all values of  $\Delta$  reproduce the observed transition for  $Bo \geq 4$  and that as  $\Delta$  decreases then the lowest value of  $Bo$  at which there is agreement becomes smaller; for  $\Delta = 1.339$  there is agreement for  $Bo \geq 1.5$ . For smaller  $Bo$ , the static model predicts the transition to be at larger values of  $D$  than the BIM model. This discrepancy is most likely explained by the fact that as  $Bo$  decreases, the amount of variation in film thickness increases (figure 34e) so the assumption of constant film thickness in the static model begins to no longer be valid. However, regardless, the modified static model still does a very good job of predicting the transition observed in the BIM, compared to the original static model (see figure 20).

## 7.2 Equilibrium Floating Position

As figure 21 shows, the equilibrium position of a floating sphere is independent of  $\lambda$ . This is an intuitive result since viscosity is only relevant for situations where fluid is moving, and floating is a static phenomenon. It is also found that as  $Bo \rightarrow 0$ , the dependence of  $z_{\text{eq}}$  on  $D$  vanishes. This is because in this limit, the gravitational forces acting to deform the interface are significantly smaller than the restorative IFT forces meaning it is very difficult to deform the fluid interface. This is why  $z_{\text{eq}} \rightarrow 1$  in this limit as this corresponds to the sphere sitting on top of a flat, undeformed interface. In the other limit (*Boinfinity*) it is only possible to consider the case  $D = 1$ , since the sphere sinks for all other values of  $D$ . Here,  $z_{\text{eq}}$  is observed to tend to the constant value of  $-0.32$ . That the equilibrium depth of the sphere is independent of the Bond number here is predicted by the modified static model described in section 7.1.3, since taking the limit of equation 83 as  $Bo \rightarrow \infty$  and setting  $D = 1$  gives

$$z_c = \frac{\Delta^{1/2}(2 + 3 \cos \theta_c - \cos^3 \theta_c)}{3 \sin^2 \theta_c}. \quad (85)$$

Equation 85 is independent of  $Bo$  so the equilibrium position of the sphere  $z_{\text{eq}} = z_c - \cos \theta_c$  is also.

## 7.3 Entrained Volume

Figures 23 and 24 show that below a critical value of  $Bo$ ,  $V \sim \ln Bo$  at a fixed  $D$  and  $\lambda$ . This result can be compared that obtained by Pitois et al. (1999) who performed experiments where steel or glass beads were dropped onto the interface between PDMS oil and water. They found that the volume of the entrained upper phase fluid was independent of  $\lambda$  (although in their experiments  $10^{-9} \leq \lambda \leq 10^{-10}$ ) and  $V \sim \ln(DBo)$ . To compare to this study, the data from figure 24 has been replotted with  $\ln(DBo)$  on the x-axis (figure 36). As can be seen, this has the effect of shifting the curves along the x-axis by an amount  $\ln D$ . It can be seen that at  $\ln(DBo) \approx 1$ , then all of the curves for different

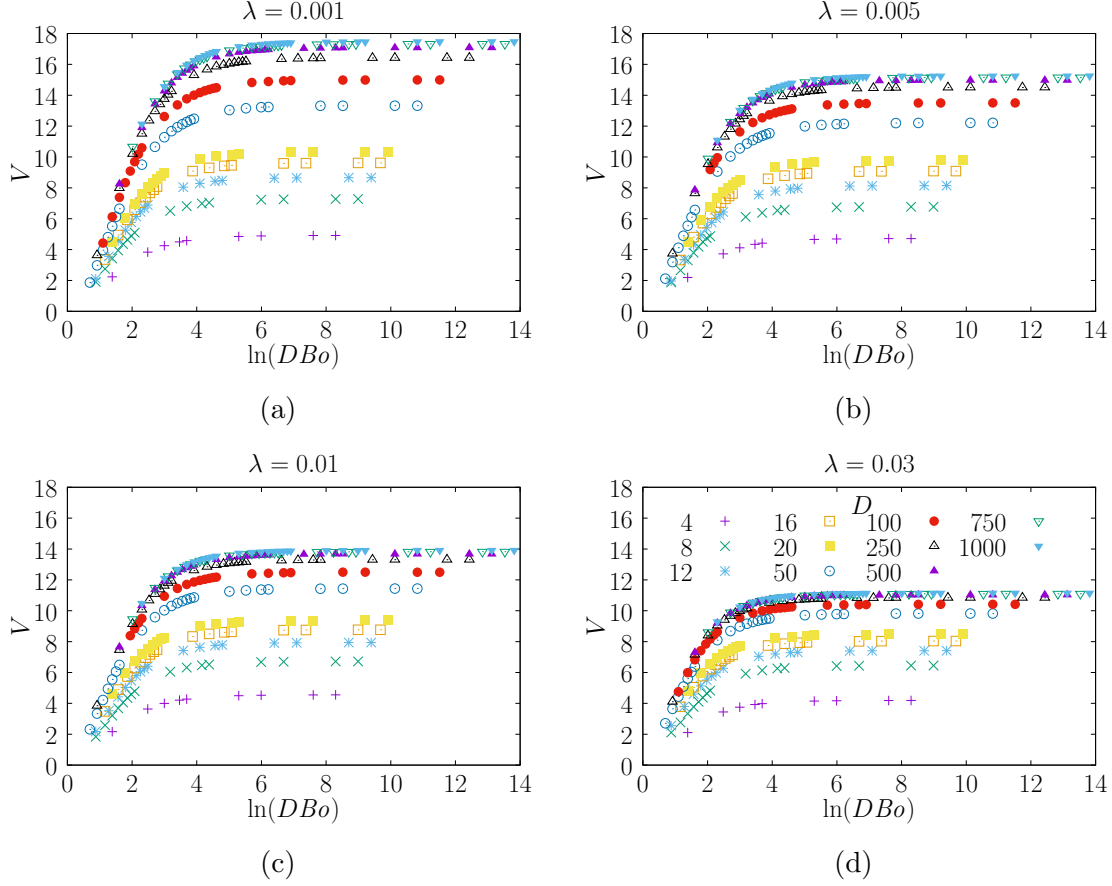


Figure 36: Dependence of entrained volume  $V$  on  $\ln(DBo)$  for different  $D$  for a)  $\lambda = 0.001$ , b)  $\lambda = 0.005$ , c)  $\lambda = 0.01$  and d)  $\lambda = 0.03$ .

values of  $D$  are coincident. However, this is generally not true. Hence the conclusion of Pitois et al. (1999) that  $V \sim \ln(DBo)$  is only valid for  $\ln(DBo) \rightarrow 1$  from above.

Our results show that for  $DBo \sim O(1) - O(10)$ , as the Bond number or MDR increase, so does the entrained volume. A qualitative explanation of this is relatively intuitive. As you increase the Bond number, the relative strength of IFT forces that oppose deformation of the interface decreases, allowing interfacial deformation further away from the sphere. By widening the field of deformation on the interface, the sphere can sink further into the lower fluid (extending the length of the column) before the column becomes so thin that it snaps. Increasing the density ratio means that, relative to the density of the sphere, the density difference between the two fluids is decreased. Hence, the buoyancy force on the upper phase fluid being dragged down into the entraining column is weaker

compared to the drag force on the fluid from the sphere. Hence, as  $D$  increases the amount of upper phase fluid entrained into the lower phase increases. It is also observed for  $DBo \sim O(1) - O(10)$  that the entrained volume is largely independent of the viscosity ratio (at least in the range  $0.001 \leq \lambda \leq 0.03$ ). Quantitatively, this is expected, since taking the limit of equation 55 as  $\lambda \rightarrow 0$  shows that dependence of the system on the viscosity ratio vanishes. A physical explanation for this can be deduced by considering a force balance on the sphere. The upward forces on the sphere are governed by the IFT and the viscosity of the two fluids. Decreasing the value of the viscosity ratio whilst keeping  $Bo$  fixed means that the IFT becomes the dominant contribution to the upward forces. Hence changes in the viscosity ratio when  $\lambda \ll 1$  have little effect on the entrained volume.

Figure 25 shows the dependence of the entrained volume  $V$  on  $\lambda$  and  $D$  for the case where  $Bo \rightarrow \infty$ . It can be seen that for  $\ln D \lesssim 2$ ,  $V \sim \ln D$ . The data in this linear regime has been fitted to the model  $V = m(\lambda) \ln D + c$  and figure 37 shows the function  $m(\lambda)$ . This relationship cannot be fitted by either an exponential or power law relationship but qualitatively,  $m(\lambda)$  decreases as  $\lambda$  increases, with  $m$  decreasing by approximately 30% over  $0.001 \leq \lambda \leq 0.05$ .

In the high  $Bo$  limit, it is seen that  $V$  is independent of  $Bo$ . This can be explained with a similar argument to above. As the Bond number decreases, so do the relative magnitudes of IFT forces. Hence, the dominant upward force on the sphere becomes the viscous drag. Once the IFT force is significantly smaller than the viscous drag, changes in the IFT force no longer affect the sphere, or the fluid entrained during sinking. This also explains why the effect of the viscosity ratio increases as the Bond number increases.

Also in the high  $Bo$  limit, for  $D \sim O(1)$ ,  $V$  is largely independent of the viscosity ratio. This is because only small viscosity ratios are considered, and the dominant control on the behaviour is the balance between the gravitational force on the sphere and the buoyant force on the fluid in the column. As  $D \rightarrow \infty$ , the upward force due to the buoyancy of the fluid in the column becomes smaller relative to the viscous drag force induced by the surrounding fluid. Hence, in this limit, the viscosity ratio becomes important.

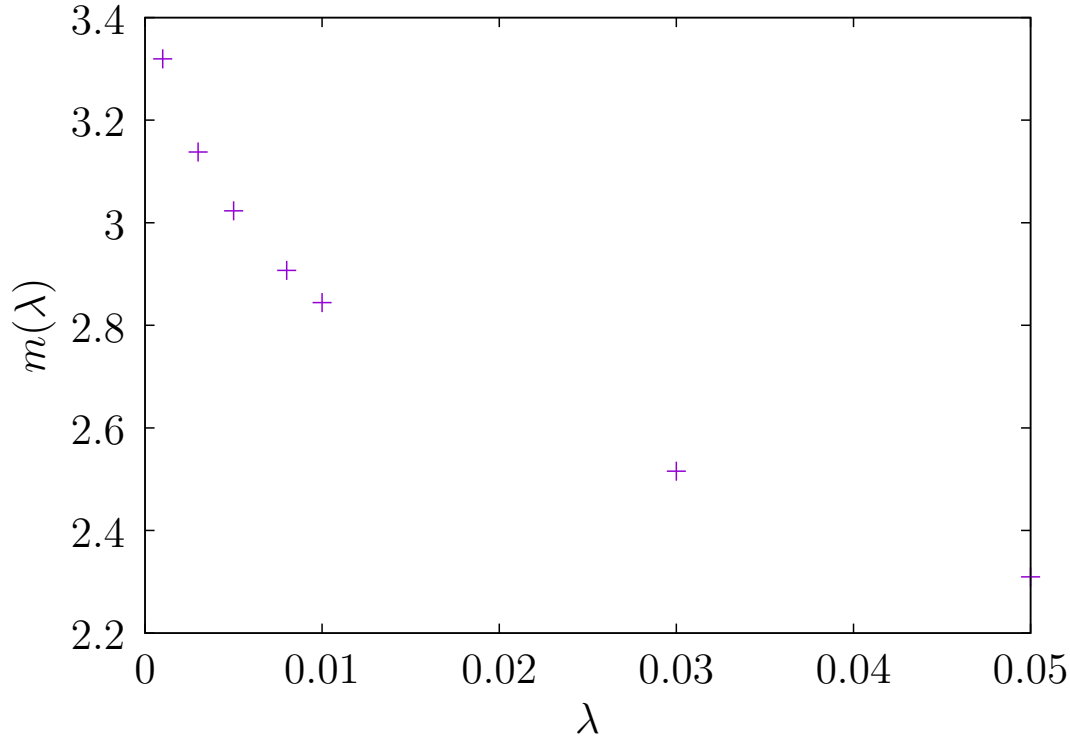


Figure 37

Larger viscosity ratios means a larger upward force on the sphere, so the sphere sinks slower, allowing the column to thin quicker than it can lengthen, thus leading to smaller entrained volumes.

Although physical principles have been able to provide a qualitative rationale for the observed results, a theoretical description providing a quantitative prediction of these results has not been attempted.

## 7.4 Sinking Timescale

As the results of section 6.1.4 show, the dependence of the sinking timescale  $t_s$  on the dimensionless parameters  $D$ ,  $Bo$  and  $\lambda$  is non-trivial. The simplest dependence is on the viscosity ratio; as  $\lambda$  increases from 0.001 to 0.03 the sinking timescale increases. This is a fairly intuitive observation; the larger the viscosity of the lower fluid the larger the drag force on the sphere and the longer the sphere takes to sink. The dependence on the

$Bo$  is significantly more complicated. As  $Bo$  tends to the floating transition,  $t_s \rightarrow \infty$ . This is to be expected as simulations where floating is observed can be interpreted as taking an infinite time to sink. Also, as  $Bo \rightarrow \infty$ ,  $t_s$  becomes independent of the Bond number. This can be explained by the fact that in this limit, the IFT forces are negligible, so viscous forces provide the dominant contribution to the upward component of force. Hence, the Bond number has no control on the rate of sinking in this regime.

The behaviour at intermediate Bond numbers is harder to explain. At  $D = 8$ , the sinking time decreases monotonically as  $Bo$  increases. However, as  $D$  increases, a minimum in  $t_s$  appears at some value of  $Bo$ . As both  $D$  and  $\lambda$  increase, the difference between the minimum sinking time, and the value of  $t_s$  as  $Bo \rightarrow \infty$  increases. This type of behaviour suggests that there is more than one process determining the rate at which the sphere sinks, with each process having a different timescale.

The sinking of a sphere can be considered to proceed in two stages: deformation and column thinning (figure 38). The deformation stage takes place from the moment the sphere first touches the plane  $z = 0$  and is characterised by the sphere deforming the interface around it as it settles through this plane. Once the sphere has moved beyond this plane, a column of upper phase fluid connects the sphere to the bulk of the upper phase. The second stage of sinking is the thinning of this column as the sphere continues to move away from the interface, dragging some of the upper phase fluid with it, whilst fluid higher in the column rises buoyantly back into the bulk of the upper phase. Once the column has thinned to a critical thickness rupture occurs.

The two stages of sinking can be considered to have intrinsic timescale associated with them,  $t_1$  for deformation and  $t_2$  for column thinning. The total sinking timescale is then given by  $t_s = t_1 + t_2$ . The effect of the dimensionless parameters on the individual timescales can be examined. The larger the viscosity ratio, the larger the viscous forces acting upward on the sphere during both stages of the sinking. Hence, increasing the value of the viscosity ratio extends both  $t_1$  and  $t_2$ . During the deformation stage, decreasing the Bond number also increases the upward force on the sphere due to the relative increase in IFT forces. Hence, decreasing  $Bo$  increases  $t_1$ . However, in the column thinning stage,

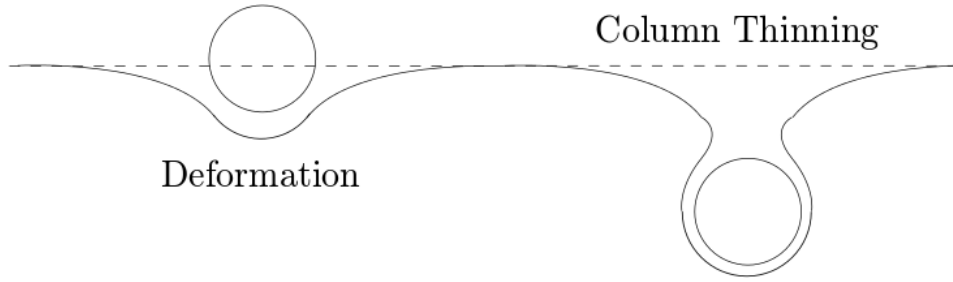


Figure 38: Two stages of a sphere sinking through an interface. Deformation: The sphere deforms the interface as it settles through the  $z = 0$  plane. Column thinning: Once the sphere is beyond the  $z = 0$  plane, a column of upper phase fluid is entrained behind the sphere. Sinking is complete once this has thinned and snapped.

a larger IFT will lead to pinching occurring at a larger column radius so a decrease in  $Bo$  decreases  $t_2$ . The opposing effects of  $Bo$  on  $t_1$  and  $t_2$  lead to the non-monotonic behaviour at intermediate Bond numbers.

A similar argument can be used to explain the similar behaviour observed in figure 27b. Increasing  $D$  decreases the density difference between the two fluid relative to that of the sphere, reducing the upward buoyancy force due to the volume of upper phase fluid displaced below the plane  $z = 0$  and so  $t_1$  decreases. However, this also means that the return velocity of the fluid in the resultant column is small and so  $t_2$  increases. This again leads to non-monotonic behaviour.

In the simulations, it is difficult to identify the time at which the deformation stage ends and the column thinning stage begins. It is therefore difficult to identify these intrinsic timescales from the data.

## 7.5 Settling Spheroids

Whilst qualitative comparisons between the behaviour of spheres and oblate spheroids, it has not been possible to produce a more quantitative comparison. The primary reason for this is that the majority of simulations involving a prolate spheroid have terminated due to



the separation between the particle and the interface becoming smaller than the distance between collocation points on either the sphere or the interface. This often occurs during the deformation phase, and so it is impossible to tell whether the particle would float or sink. Additionally, if the simulation does proceed to the column-thinning stage, the particle-interface separation criteria is satisfied long before the interface snapping criteria meaning no data regarding the sinking timescale or the entrained volume can be obtained.

## A Dirac Delta Function

In a volume  $\mathcal{V}$  bounded by a surface  $\mathcal{S}$ , the Dirac delta function  $\delta(\mathbf{x} - \mathbf{y})$  is defined as (Riley et al., 2006)

$$\int_{\mathcal{V}} f(\mathbf{y}) \delta(\mathbf{x} - \mathbf{y}) d^3 \mathbf{y} = \begin{cases} f(\mathbf{x}), & \mathbf{x} \in \mathcal{V} \\ \frac{f(\mathbf{x})}{2}, & \mathbf{x} \in \mathcal{S} \\ 0, & \text{otherwise} \end{cases}. \quad (86)$$

The result for  $\mathbf{x} \in \mathcal{S}$  is only valid for the case that the surface is Lyapunov smooth (a local tangent plane exists everywhere) (Gunter, 1967). Equation 86 means that

$$\int_{\mathcal{V}} \delta(\mathbf{x} - \mathbf{y}) d^3 \mathbf{y} = 1, \quad \mathbf{x} \in \mathcal{V}. \quad (87)$$

A key property of the delta function is that it is symmetric under a change of sign of the argument;

$$\delta(-\mathbf{x}) = \delta(\mathbf{x}). \quad (88)$$

It also needs to be noted that the Dirac delta function can be expressed as (Riley et al.,

2006)

$$\delta(\boldsymbol{\xi}) = \frac{1}{(2\pi)^3} \int e^{i\mathbf{k} \cdot \boldsymbol{\xi}} d^3\mathbf{k}, \quad (89)$$

where  $\mathbf{k}$  is the transform variable and  $i$  is the imaginary unit.

## B Greens Functions for Stokes Flow

We present here a derivation of equations 31 and 32 following Ladyzhenskaya (1963). First, the Greens function for dynamic pressure  $\hat{P}(\boldsymbol{\xi})$  is defined such that

$$\hat{T}_{ij}(\boldsymbol{\xi}) = -\hat{P}(\boldsymbol{\xi})\delta_{ij} + \Lambda[\partial'_i \hat{u}_j(\boldsymbol{\xi}) + \partial'_j \hat{u}_i(\boldsymbol{\xi})]. \quad (90)$$

Substituting this into equation 30, and using equation 29 yields

$$-\partial'_j \hat{P}(\boldsymbol{\xi}) + \Lambda \partial'_i \partial'_i \hat{u}_j(\boldsymbol{\xi}) + \mathcal{F}_j \delta(\boldsymbol{\xi}) = 0. \quad (91)$$

We also define two further quantities,  $\bar{P}_i$  and  $\bar{u}_{ij}$  such that

$$\hat{P}(\boldsymbol{\xi}) = \mathcal{F}_i \bar{P}_i(\boldsymbol{\xi}), \quad (92)$$

and

$$\hat{u}_j(\boldsymbol{\xi}) = \mathcal{F}_i \bar{u}_{ij}(\boldsymbol{\xi}). \quad (93)$$

Substitution of these expressions into equations 29 and 91, and rearranging results in

$$\partial'_i \bar{u}_{ij}(\boldsymbol{\xi}) = 0, \quad (94)$$

and

$$-\partial'_j \bar{P}_i(\boldsymbol{\xi}) + \Lambda \partial'_k \partial'_k \bar{u}_{ij}(\boldsymbol{\xi}) + \delta_{ij} \delta(\boldsymbol{\xi}) = 0. \quad (95)$$

To derive functional forms for the Greens functions, it is necessary to express equations 94 and 95 in Fourier representation. To do this we need to define the Fourier transformed variables  $\tilde{P}_{\alpha,i}$  and  $\tilde{u}_{\alpha,ij}$  (Riley et al., 2006):

$$\bar{P}_i(\boldsymbol{\xi}) = \frac{1}{(2\pi)^{3/2}} \int \tilde{P}_i(\mathbf{k}) e^{i\mathbf{k} \cdot \boldsymbol{\xi}} d^3 \mathbf{k}, \quad (96)$$

and

$$\bar{u}_{ij}(\boldsymbol{\xi}) = \frac{1}{(2\pi)^{3/2}} \int \tilde{u}_{ij}(\mathbf{k}) e^{i\mathbf{k} \cdot \boldsymbol{\xi}} d^3 \mathbf{k}. \quad (97)$$

where  $\mathbf{k}$  is the transform variable, and  $i$  is the unit imaginary number. Substitution of these, and the Fourier definition of the Dirac delta function (equation 89 in appendix A) into equations 94 and 95 gives the Fourier representations of the continuity and Stokes equations respectively. Following some manipulation these can be written as

$$k_i \tilde{u}_{ij}(\mathbf{k}) = 0, \quad (98)$$

and

$$-ik_j \tilde{P}_i(\mathbf{k}) - \Lambda k^2 \tilde{u}_{ij}(\mathbf{k}) + \frac{\delta_{ij}}{(2\pi)^{3/2}} = 0. \quad (99)$$

where  $k = k_i k_i$ . By contracting equation 99 with  $k_j$ , substituting in equation 98, and rearranging, it is then possible to obtain the Fourier representation of the Greens function

for pressure;

$$\tilde{P}_i(\mathbf{k}) = \frac{-ik_i}{(2\pi)^{3/2}k^2}. \quad (100)$$

A final substitution of this into equation 96 gives the Greens function for pressure;

$$\bar{P}_i(\boldsymbol{\xi}) = \frac{-i}{(2\pi)^3} \int \frac{k_i e^{i\mathbf{k} \cdot \boldsymbol{\xi}} d^3 \mathbf{k}}{k^2}. \quad (101)$$

This integral is evaluated in appendix B.1 and it is shown that

$$\bar{P}_i(\boldsymbol{\xi}) = -\frac{1}{4\pi} \partial'_i \left( \frac{1}{\xi} \right) = \frac{\xi_i}{4\pi \xi^3} \quad , \quad \xi = \xi_i \xi_i. \quad (102)$$

We also need to find an equivalent expression for  $\bar{u}_{ij}$ . To do so, substitute equation 100 into equation 99 and rearrange;

$$\tilde{u}_{ij}(\mathbf{k}) = \frac{k^2 \delta_{ij} - k_i k_j}{(2\pi)^{3/2} k^4 \Lambda}. \quad (103)$$

Combining this with equation 97 results in an expression for the Greens function for velocity;

$$\bar{u}_{ij}(\boldsymbol{\xi}) = \frac{1}{(2\pi)^3 \Lambda} \left( \delta_{ij} \int \frac{e^{i\mathbf{k} \cdot \boldsymbol{\xi}} d^3 \mathbf{k}}{k^2} - \int \frac{k_i k_j e^{i\mathbf{k} \cdot \boldsymbol{\xi}} d^3 \mathbf{k}}{k^4} \right). \quad (104)$$

These integrals are evaluated in appendix B.2 (equations 118 and 124) and following some manipulation we find

$$\bar{u}_{ij}(\boldsymbol{\xi}) = \frac{1}{8\pi \Lambda \xi} \left( \delta_{ij} + \frac{\xi_i \xi_j}{\xi^2} \right). \quad (105)$$

We can now substitute equations 102 and 105 into 92 and 93 to obtain

$$\hat{P}(\boldsymbol{\xi}) = \frac{\mathcal{F}_i \xi_i}{4\pi \xi^3}, \quad (106)$$

and

$$\hat{u}_j(\boldsymbol{\xi}) = \frac{\mathcal{F}_i}{8\pi \Lambda_\alpha \xi} \left( \delta_{ij} + \frac{\xi_i \xi_j}{\xi^2} \right). \quad (107)$$

Substitution of equations 106 and 107 into equation 90 results in

$$\hat{T}_{ij}(\boldsymbol{\xi}) = \frac{-3\mathcal{F}_k \xi_i \xi_j \xi_k}{4\pi \xi^5}. \quad (108)$$

The kernels  $J_{ij}$  and  $K_{ijk}$  are defined as

$$J_{ij} = \frac{1}{8\pi \xi} \left( \delta_{ij} + \frac{\xi_i \xi_j}{\xi^2} \right), \quad (109)$$

and

$$K_{ijk} = \frac{-3\xi_i \xi_j \xi_k}{4\pi \xi^5}. \quad (110)$$

Hence we obtain the Greens functions for the velocity and stress fields (equations 31 and 32). Note that under the interchange  $\boldsymbol{\xi} \rightarrow -\boldsymbol{\xi}$  the kernels are symmetric and anti-symmetric respectively;

$$J_{ki}(-\boldsymbol{\xi}) = J_{ki}(\boldsymbol{\xi}), \quad (111)$$

$$K_{jik}(-\boldsymbol{\xi}) = -K_{jik}(\boldsymbol{\xi}). \quad (112)$$

## B.1 Integral for Greens Function for Pressure

Here we present a proof of the evaluation of the integral in equation 101. First recall the identity (Jackson, 1999; Frahm, 1982)

$$\partial_i \partial_i \left( \frac{1}{\xi} \right) = -4\pi \delta(\boldsymbol{\xi}). \quad (113)$$

Substituting in the Fourier definition of the delta function (equation 89) leads to

$$\partial_i \partial_i \left( \frac{1}{\xi} \right) = \frac{-4\pi}{(2\pi)^3} \int e^{i\mathbf{k} \cdot \boldsymbol{\xi}} d^3 \mathbf{k}. \quad (114)$$

Inspection of this then suggests

$$\partial_i \left( \frac{1}{\xi} \right) = \frac{4i\pi}{(2\pi)^3} \int \frac{k_i e^{i\mathbf{k} \cdot \boldsymbol{\xi}} d^3 \mathbf{k}}{k^2}. \quad (115)$$

Hence

$$\frac{-i}{(2\pi)^3} \int \frac{k_i e^{i\mathbf{k} \cdot \boldsymbol{\xi}} d^3 \mathbf{k}}{k^2} = -\frac{1}{4\pi} \partial_i \left( \frac{1}{\xi} \right). \quad (116)$$

## B.2 Integrals for the Greens Function for Velocity

Here we present proofs of the evaluation of the two integrals in equation 104. For the first integral, inspection of equation 115 in appendix B.1 shows

$$\frac{1}{\xi} = \frac{4\pi}{(2\pi)^3} \int \frac{e^{i\mathbf{k} \cdot \boldsymbol{\xi}} d^3 \mathbf{k}}{k^2}. \quad (117)$$

Hence the first integral in equation 104 is

$$\int \frac{e^{i\mathbf{k}\cdot\boldsymbol{\xi}} d^3\mathbf{k}}{k^2} = \frac{(2\pi)^3}{4\pi\xi}. \quad (118)$$

The second integral requires a bit more work. Firstly, express it in a different form;

$$\int \frac{k_i k_j e^{i\mathbf{k}\cdot\boldsymbol{\xi}} d^3\mathbf{k}}{k^4} = \partial_i \partial_j \left( \int \frac{e^{i\mathbf{k}\cdot\boldsymbol{\xi}} d^3\mathbf{k}}{k^4} \right). \quad (119)$$

To evaluate this, first consider  $\nabla^4 \xi = \nabla^2(\nabla^2 \xi)$ . Expanding  $\nabla^2$  in spherical polar coordinates centred on  $\xi = 0$  shows

$$\nabla^4 \xi = 2\nabla^2 \left( \frac{1}{\xi} \right). \quad (120)$$

Combining this with equation 114 we obtain

$$\nabla^4 \xi = \frac{-8\pi}{(2\pi)^3} \int e^{i\mathbf{k}\cdot\boldsymbol{\xi}} d^3\mathbf{k}. \quad (121)$$

Inspection of this yields

$$\xi = \frac{-8\pi}{(2\pi)^3} \int \frac{e^{i\mathbf{k}\cdot\boldsymbol{\xi}} d^3\mathbf{k}}{k^4}. \quad (122)$$

Rearranging this produces an expression for the integral on the right hand side of equation 119;

$$\int \frac{e^{i\mathbf{k}\cdot\boldsymbol{\xi}} d^3\mathbf{k}}{k^4} = -\frac{(2\pi)^3 \xi}{8\pi}. \quad (123)$$

Hence

$$\int \frac{k_i k_j e^{i\mathbf{k} \cdot \boldsymbol{\xi}} d^3 \mathbf{k}}{k^4} = \frac{(2\pi)^3 \partial'_i \partial'_j \xi}{8\pi}. \quad (124)$$

## C Lorentz Reciprocal Theorem

Consider a pair of velocity fields  $u_i$  and  $u'_i$ , and a pair of stress fields  $T_{ij}$  and  $T'_{ij}$  defined over a domain  $\mathcal{V}$  bounded by a surface  $\mathcal{S}$  with normal  $n_i$ . Now suppose that both  $u_i$  and  $T_{ij}$ , and  $u'_i$  and  $T'_{ij}$  are both solutions to the Stokes equations with a point source term (equations 29 and 30). The Lorentz reciprocal theorem then states that (Kim and Karrila, 2005)

$$\begin{aligned} \oint_{\mathcal{S}} n_j(\mathbf{x}') T'_{ij}(\mathbf{x}') \hat{u}_i(\boldsymbol{\xi}) d\mathbf{x}'^2 - \oint_{\mathcal{V}} [\partial'_j T'_{ij}(\mathbf{x}')] \hat{u}_i(\boldsymbol{\xi}) d\mathbf{x}'^3 &= \oint_{\mathcal{S}} n_j(\mathbf{x}') \hat{T}_{ij}(\boldsymbol{\xi}) u'_i(\mathbf{x}') d\mathbf{x}'^2 \\ &\quad - \oint_{\mathcal{V}} [\partial'_j \hat{T}_{ij}(\boldsymbol{\xi})] u'_i(\mathbf{x}') d\mathbf{x}'^3. \end{aligned} \quad (125)$$

Our definition of the theorem has defined the integrals in the sense of the Cauchy Principle Value (CPV) (appendix D) to allow for the case that one or more of the fields may be singular at some point in the domain (as in the case of Greens functions). For the case that all of the fields are regular, then the CPV integral just evaluates to the regular integral. In the proof of equation 125 given by Kim and Karrila (2005) it is straightforward to extend their result to ours just by taking care when defining the integrals.

## D Cauchy Principle Value

Consider a function  $f(x)$  such that  $f(x \rightarrow x_0) \rightarrow \infty$ . Hence we need to take care when defining an integral of  $f(x)$  over a range which contains  $x_0$ . We denote the Cauchy



Principle Value of an integral with a horizontal line through the integral sign, and for a singularity at the point  $x_0$  it is defined such that (Boas, 1983)

$$\oint_a^b f(x)dx = \lim_{\epsilon \rightarrow 0} \left( \int_a^{x_0-\epsilon} f(x)dx + \int_{x_0+\epsilon}^b f(x)dx \right) \quad (126)$$

This can be readily extended to higher dimensional integrals by performing the integration everywhere except in a small region around the singular point, and then finding the limiting value of the integral as the size of that region tends to zero. Also, for the case that the function is actually regular throughout this region, then the CPV equates to the standard integral.

## E Divergence Theorem

The divergence theorem states that for a volume  $\mathcal{V}$  bounded by a surface  $\mathcal{S}$  with outward normal  $n_i$ , then for a continuous and differentiable vector field  $a_i$  (Riley et al., 2006)

$$\int_{\mathcal{V}} \partial_i a_i d\mathcal{V} = \oint_{\mathcal{S}} a_i n_i d\mathcal{S}. \quad (127)$$

## F Elliptic Integrals

The complete elliptic integrals of the first and second kind are defined as (Abramowitz and Stegun, 1972)

$$K(k^2) = \int_0^{\pi/2} \frac{d\theta}{(1 - k^2 \sin^2 \theta)^{1/2}}, \quad 0 \leq k^2 < 1, \quad (128)$$

Table 3: The coefficients for equations 130 and 131.

$a_0$	1.38629436112	$b_0$	0.5
$a_1$	0.09666344259	$b_1$	0.12498593597
$a_2$	0.03590092383	$b_2$	0.06880248576
$a_3$	0.03742563713	$b_3$	0.03328355346
$a_4$	0.01451196212	$b_4$	0.00441787012
$a'_1$	0.44325141463	$b'_1$	0.24998368310
$a'_2$	0.06260601220	$b'_2$	0.09200180037
$a'_3$	0.04757383546	$b'_3$	0.04069697526
$a'_4$	0.01736506451	$b'_4$	0.00526449639

and

$$E(k^2) = \int_0^{\pi/2} (1 - k^2 \sin^2 \theta)^{1/2} d\theta, \quad 0 \leq k^2 < 1, \quad (129)$$

where  $k^2$  is termed the modulus of the integral. Polynomial approximations can be found to evaluate the integrals (Roumeliotis, 2000) and we use the following expressions from Abramowitz and Stegun (1972):

$$K(k^2) = \sum_{i=0}^4 a_i (1 - k^2)^i + \ln \left( \frac{1}{1 - k^2} \right) \sum_{i=0}^4 b_i (1 - k^2)^i, \quad (130)$$

$$E(k^2) = 1 + \sum_{i=1}^4 a'_i (1 - k^2)^i + \ln \left( \frac{1}{1 - k^2} \right) \sum_{i=1}^4 b'_i (1 - k^2)^i \quad (131)$$

The values of the coefficients in the expansion are in table 3.

## **G Components of *A*, *B* and *C***

Here we present expressions for the components of *A*, *B* and *C* in terms of complete elliptic integrals of the first and second kind (appendix F). The expressions for *A* and *B* are from Graziani (1989) although our notation is more similar to that of Manga (1994). As far as the authors are aware, equivalent expressions for *C* have never been published before, although they were undoubtedly used in the models of Lee and Leal (1982), Geller et al. (1985), Manga and Stone (1995) and Roumeliotis (2000). The quantities  $\alpha$  and  $\beta$  are defined as (Manga, 1994)

$$\alpha^2 = x_r^2 + y_r^2 + (x_z - y_z)^2, \quad (132)$$

and

$$\beta^2 = 2x_r y_r. \quad (133)$$

$K$  and  $E$  are complete elliptic integrals of the first and second kind respectively and they all take  $k^2 = 2\beta^2/(\alpha^2 + \beta^2)$  as their modulus.

The components of *A* are:

$$A_{11} = (c_1 n_r + c_2 n_z)K(k^2) + (c_3 n_r + c_4 n_z)E(k^2), \quad (134)$$

$$A_{12} = (c_2 n_r + c_6 n_z)K(k^2) + (c_4 n_r + c_8 n_z)E(k^2), \quad (135)$$

$$A_{21} = (c_9 n_r + c_{10} n_z)K(k^2) + (c_{11} n_r + c_{12} n_z)E(k^2), \quad (136)$$

and

$$A_{22} = (c_{10}n_r + c_{14}n_z)K(k^2) + (c_{12}n_r + c_{16}n_z)E(k^2). \quad (137)$$

The coefficients  $c_i$  are given as

$$c_1 = \frac{(1 - \lambda)[x_r\alpha^2(4\alpha^4 - 18x_r^2y_r^2) - x_r(2y_r^2 + x_r^2)(2\alpha^4 - 3\beta^4) - y_r\alpha^2\beta^2(y_r^2 + 2x_r^2) + x_ry_r^2\beta^4]}{\pi(\alpha^2 + \beta^2)^{3/2}(\alpha^2 - \beta^2)\beta^4}, \quad (138)$$

$$c_2 = \frac{(1 - \lambda)(x_z - y_z)[2\alpha^4 - 2\beta^4 - \alpha^2(x_z - y_z)^2]}{\pi(\alpha^2 + \beta^2)^{3/2}(\alpha^2 - \beta^2)\beta^2}, \quad (139)$$

$$c_3 = \frac{1 - \lambda}{\pi(\alpha^2 + \beta^2)^{3/2}(\alpha^2 - \beta^2)^2\beta^4} \left( \frac{x_r(-8\alpha^8 + 15\alpha^4\beta^4 - 3\beta^8)}{2} - 2x_r\alpha^2(2y_r^2 + x_r^2)(-\alpha^4 + 3\beta^4) + y_r\beta^2(y_r^2 + 2x_r^2)(\alpha^4 + 3\beta^4) - 4x_ry_r^2\alpha^2\beta^4 \right), \quad (140)$$

$$c_4 = \frac{-(1 - \lambda)(x_z - y_z)}{\pi(\alpha^2 + \beta^2)^{3/2}(\alpha^2 - \beta^2)^2\beta^2} (\alpha^4(\alpha^4 - 5\beta^4) + [\alpha^2 - (x_z - y_z)^2](\alpha^4 + 3\beta^4)), \quad (141)$$

$$c_6 = \frac{(1 - \lambda)(x_z - y_z)^2(2x_r^2 - \alpha^2)}{2\pi(\alpha^2 + \beta^2)^{3/2}(\alpha^2 - \beta^2)x_r}, \quad (142)$$

$$c_8 = \frac{(1 - \lambda)(x_z - y_z)^2(\alpha^4 + 3\beta^4 - 8x_r^2\alpha^2)}{2\pi(\alpha^2 + \beta^2)^{3/2}(\alpha^2 - \beta^2)^2x_r}, \quad (143)$$

$$c_9 = \frac{(1 - \lambda)(x_z - y_z)(-2\alpha^4 + 3\beta^4 - 4y_r^2\alpha^2 + 4y_r^4)}{4\pi(\alpha^2 + \beta^2)^{3/2}(\alpha^2 - \beta^2)y_r}, \quad (144)$$

$$c_{10} = \frac{(1 - \lambda)(x_z - y_z)^2(\alpha^2 - 2y_r^2)}{2\pi(\alpha^2 + \beta^2)^{3/2}(\alpha^2 - \beta^2)y_r}, \quad (145)$$

$$c_{11} = \frac{(1 - \lambda)(x_z - y_z)(\alpha^6 - 3\alpha^2\beta^4 + 2y_r^2\alpha^4 + 6y_r^2\beta^4 - 8y_r^4\alpha^2)}{2\pi(\alpha^2 + \beta^2)^{3/2}(\alpha^2 - \beta^2)^2y_r^2}, \quad (146)$$

$$c_{12} = \frac{(1 - \lambda)(x_z - y_z)^2(8y_r^2\alpha^2 - \alpha^4 - 3\beta^4)}{2\pi(\alpha^2 + \beta^2)^{3/2}(\alpha^2 - \beta^2)y_r}, \quad (147)$$

$$c_{14} = \frac{(1 - \lambda)(x_z - y_z)^3}{\pi(\alpha^2 + \beta^2)^{3/2}(\alpha^2 - \beta^2)}, \quad (148)$$

and

$$c_{16} = \frac{-4(1 - \lambda)(x_z - y_z)^3\alpha^2}{\pi(\alpha^2 + \beta^2)^{3/2}(\alpha^2 + \beta^2)^2}. \quad (149)$$

The components of  $\mathbf{B}$  are:

$$B_{11} = \frac{1}{2\pi\beta^2(\alpha^2 + \beta^2)^{1/2}} \left[ [\alpha^2 + (x_z - y_z)^2]K - \left( \alpha^2 + \beta^2 + \frac{\alpha^2(x_z - y_z)^2}{\alpha^2 - \beta^2} \right) E \right], \quad (150)$$

$$B_{12} = \frac{x_z - y_z}{4\pi x_r(\alpha^2 + \beta^2)^{1/2}} \left( \frac{(2x_r^2 - \alpha^2)E}{\alpha^2 - \beta^2} + K \right), \quad (151)$$

$$B_{21} = \frac{x_z - y_z}{4\pi y_r(\alpha^2 + \beta^2)^{1/2}} \left( \frac{(\alpha^2 - 2y_r^2)E}{\alpha^2 - \beta^2} - K \right), \quad (152)$$

and

$$B_{22} = \frac{1}{2\pi(\alpha^2 + \beta^2)^{1/2}} \left( K + \frac{(x_z - y_z)^2 E}{\alpha^2 - \beta^2} \right). \quad (153)$$

The components of  $\mathbf{C}$  are:

$$C_1 = \frac{9(\partial'_j n_j - y_z \text{Bo})}{4\pi D \text{Bo}(\alpha^2 + \beta^2)^{1/2}} \left[ \left( [\alpha^2 + (x_z - y_z)^2] n_r + y_r (x_z - y_z) \right) K \right. \\ \left. + \frac{E}{\alpha^2 - \beta^2} \left( n_r [\beta^4 - \alpha^2(\alpha^2 + (x_z - y_z)^2)] + n_z (x_z - y_z) (x_r \beta^2 - y_r \alpha^2) \right) \right], \quad (154)$$

and

$$C_2 = \frac{9(\partial'_j n_j - y_z \text{Bo})}{4\pi D \text{Bo}(\alpha^2 + \beta^2)^{1/2}} \left( [\beta^2 n_z - x_r (x_z - y_z) n_r] K \right. \\ \left. + \frac{[n_r (x_r \alpha^2 - y_r \beta^2) + (x_z - y_z) \beta^2 n_z] (x_z - y_z) E}{\alpha^2 - \beta^2} \right). \quad (155)$$

### G.1 Special case: $x_r = 0$

For the special case that the point  $\mathbf{x}'$  is on the axis of symmetry ( $x_r = 0$ ) then expressions can be found for the components of  $\mathbf{A}$ ,  $\mathbf{B}$  and  $\mathbf{C}$  that don't depend on elliptic integrals. Hence, in this scenario the components can be evaluated exactly and don't need to be approximated by polynomials. In this case the components of  $\mathbf{A}$  are

$$A_{11} = A_{12} = 0, \quad (156)$$

$$A_{21} = \frac{3(1 - \lambda)(x_z - y_z) y_r [(x_z - y_z) n_z - y_r n_r]}{2\alpha^5}, \quad (157)$$

and

$$A_{22} = \frac{3(1 - \lambda)(x_z - y_z)^2 [y_r n_r - (x_z - y_z) n_z]}{2\alpha^5}. \quad (158)$$

The components of  $\mathbf{B}$  are

$$B_{11} = B_{12} = 0, \quad (159)$$

$$B_{21} = \frac{-(x_z - y_z)y_r}{4\alpha^3}, \quad (160)$$

and

$$B_{22} = \frac{1}{4\alpha} \left( 1 + \frac{(x_z - y_z)^2}{\alpha^2} \right). \quad (161)$$

Finally the components of  $\mathbf{C}$  are

$$C_1 = 0, \quad (162)$$

and

$$C_2 = \frac{9(\partial'_i n_i - \text{Bo} y_z)}{8D\text{Bo}\alpha} \left( 1 + \frac{(x_z - y_z)^2}{\alpha^2} \right). \quad (163)$$

## References

- Milton Abramowitz and Irene A. Stegun. *Handbook of Mathematical Functions*. Dover, tenth edition, 1972.
- G. K. Batchelor. *An Introduction to Fluid Dynamics*. Cambridge University Press, first edition, 1967.
- M. L. Boas. *Mathematical methods in the physical sciences*. Wiley, second edition, 1983.
- J.U. Brackbill, D.B. Kothe, and C. Zemach. A Continuum Method for Modeling Surface Tension. *Journal of Computational Physics*, 100:334 – 354, 1992.
- E. B. V. Dussan. The moving contact line: the slip boundary condition. *Journal of Fluid Mechanics*, 77:665–684, 1976.

- Charles P. Frahm. Some novel delta-function identities. *Americal Journal of Physics*, 51: 826–829, 1982.
- Mark Galassi, Jim Davies, James Theiler, Brian Gough, Gerard Jungman, Patrick Alken, Michael Booth, and Fabrice Rossi. *GNU Scientific Library Reference Manual*. Network Theory Ltd., third edition, 2009.
- G. Galilei. *Discourse on bodies in water*. William Leybourn, second edition, 1663.
- A. S. Geller, S. H. Lee, and L. G. Leal. The creeping motion of a spherical particle normal to a deformable interface. *Journal of Fluid Mechanics*, 169:27–69, 1985.
- J. Willard Gibbs. On the Equilibrium of Heterogeneous Substances. Part II. *Transactions of the Connecticut Academy of Arts and Sciences*, 3:343–524, 1878.
- G. Graziani. A boundary integral equation method for axisymmetric viscous flows. *International Journal of Engineering Science*, 27:855–864, 1989.
- N. M. Gunter. *Potential Theory and Its Applications to Basic Problems of Mathematical Physics*. Frederick Ungar Publishing Company, first edition, 1967.
- J. Happel and H. Brenner. *Low Reynolds number hydrodynamics*. Noordhoff International Publishing, second edition, 1973.
- S. Hartland. The Approach of a Rigid Sphere to a Deformable Liquid/Liquid Interface. *Journal of Colloid and Interface Science*, 26:383–394, 1968.
- John David Jackson. *Classical electrodynamics*. Wiley, 3rd edition, 1999.
- A. F. Jones and S. D. R. Wilson. The film drainage problem in droplet coalescence. *Journal of Fluid Mechanics*, 87:263–288, 1978.
- Joseph B. Keller. Surface tension force on a partly submerged body. *Physics of Fluids*, 10:3009–3010, 1998.
- Sangtae Kim and Seppo J. Karrila. *Microhydrodynamics: Principles and Selected Applications*. Dover Publications, second edition, 2005.



- O. A. Ladyzhenskaya. *The Mathematical Theory of Viscous Incompressible Flow*. Gordon and Breach, first edition, 1963.
- S. H. Lee and L. G. Leal. The Motion of a Sphere in the Presence of a Deformable Interface II. A Numerical Study of the Translation of a Sphere Normal to an Interface. *Journal of Colloid and Interface Science*, 87:81–106, 1982.
- Michael Manga. *The motion of deformable drops and bubbles at low Reynolds number: Applications to selected problems in geology and geophysics*. PhD thesis, Harvard University, 1994.
- Michael Manga and H. A. Stone. Low Reynolds number motion of bubbles, drops and rigid spheres through fluid-fluid interfaces. *Journal of Fluid Mechanics*, 287:279–298, 1995.
- J. C. Maxwell. On Stresses in Rarefied Gases Arising from Inequalities in Temperature. *Philosophical Transactions of the Royal Society of London*, 170:231–256, 1879.
- Olivier Pitois, Pascal Moucheront, and Claire Weill. Franchissement d’interface et enrobage d’une sphère. *C. R. Acad. Sci. Paris*, 327:605–611, 1999.
- C. Pozrikids. *Boundary integral and singularity methods for linearized viscous flows*. Cambridge University Press, first edition, 1992.
- William H. Press, Saul A. Teukolsky, William T. Vetterling, and Brian P. Flannery. *Numerical Recipes: The Art of Scientific Computing*. Cambridge University Press, third edition, 2007.
- Osborne Reynolds. On the Theory of Lubrication and its Application to Mr Beauchamp Tower’s Experiments, including an Experimental Determination of the Viscosity of Olive Oil. *Philosophical Transactions of the Royal Society of London*, 177:157–234, 1886.
- K. F. Riley, M. P. Hobson, and S. J. Bence. *Mathematical Methods for Physics and Engineering*. Cambridge University Press, third edition, 2006.

- John Roumeliotis. *A Boundary Integral Method Applied to Stokes Flow*. PhD thesis, University of New South Wales, 2000.
- James Thomson. On certain curious Motions observable at the Surfaces of Wine and other Alcoholic Liquors. *Philosophical Magazine Series 4*, 10:330–333, 1855.
- Dominic Vella and Jie Li. The impulsive motion of a small cylinder at an interface. *Physics of Fluids*, 22, 2010.
- Dominic Vella and Paul D. Metcalfe. Surface tension dominated impact. *Physics of Fluids*, 19, 2007.
- Dominic Vella, Duck-Gyu Lee, and Ho-Young Kim. The Load Supported by Small Floating Objects. *Langmuir*, 22:5979–5981, 2006.
- Dominic Joseph Robert Vella. *The Fluid Mechanics of Floating and Sinking*. PhD thesis, University of Cambridge, 2007.
- Frank M. White. *Fluid Mechanics*. McGraw Hill, seventh edition, 1999.